Ref. Ares(2024)718080 - 31/01/2024

SEMANTIC

end-to-end Slicing and data-drivEn autoMAtion of Next generation cellular neTworks with mobIle edge Clouds

Marie Skłodowska-Curie Actions (MSCA)
Innovative Training Networks (ITN)
H2020-MSCA-ITN-2019
861165 – SEMANTIC

WP1 – Spectrum and Forward-Compatibility Aspects for multi-GHz NR operation

D1.3: Performance Evaluation and Experimentation (M49)

Contractual Date of Delivery:	M49
Actual Date of Delivery:	25/01/2024
Responsible Beneficiary:	NI
Contributing beneficiaries:	NI, CLM, UOA
Security:	Public
Nature:	Report
Version:	V1.0

Document Information

Version Date: 25/01/2024
Total Number of Pages: 73

Authors

Name	Organization	Email
Dr. Abdo Gaber	NI	abdo.gaber@ni.com
Muhammad Qurratulain Khan	NI	muhammad.qurratulain.khan@ni.com
Prof. Tommy Svensson	CLM	tommy.svensson@chalmers.se
Azadeh Tabeshnezhad	CLM	azadeh.tabeshnezhad@chalmers.se
Mehdi Sattari	CLM	mehdi.sattari@chalmers.se
Dr. Nikos Passas	UOA	passas@di.uoa.gr
Ayham Alyosef	UOA	aalyosef@di.uoa.gr
Dr. Dionysis Xenakis	FOG	dionysis@fogus.gr

Document History

Revision	Date	Modification	Contact Person
V0.1	10/10/2023	Preliminary table of contents	Dr. Abdo Gaber
V0.2	05/12/2023	Integrate the inputs from WP1 members into a single document	Muhammad Qurratulain Khan
V0.3	04/01/2024	Overall corrections, improve readability, structure update, and address list of suggestions	Dr. Abdo Gaber

V0.4	11/01/2024	Integrate updates from WP1 members to deliverable	Muhammad Qurratulain Khan
V0.5	15/01/2024	Review recent updates	Dr. Abdo Gaber
V1.0	25/01/2024	Document finalization	Dr. Abdo Gaber

TABLE OF CONTENTS

List of Acronyms and Abbreviations

Abbreviation	**Explanation**
3GPP	3rd generation partnership project
5G	5th generation of wireless networks
6G	6th generation of wireless networks
ADC	Analogue to digital converter
AF	Amplify-and-forward
AOA	Angle of arrival
A-RIS	Absorptive RIS
AS	Angular Spread
BN	Batch normalization
BM	Beam management
BS	Base station
CDF	Cumulative distribution function
CCDF	Complementary cumulative density function
CDL	Clustered Delay Line
CLM	Chalmers University of Technology
CNN	Convolutional neural network
CSI	Channel state information
DMRS	Demodulation Reference Signal
DNN	Deep neural network
DL	Downlink
DQN	Deep Q-network
DRL	Deep RL
DoF	Degree of freedom
EBS	Exhaustive beam search
EM	Electromagnetic
ESR	Early-stage researcher
FCNN	Fully convolutional neural network
FD	Full duplex
FHPPP	Finite homogeneous PPP
GA	Genetic algorithm
GPS	Global positioning system
HBS	Hierarchical beam search
IAB	Integrated access and backhaul
IOT	Internet of things
IRA	Integrated resource allocation
KNN	K-nearest neighbors
LDPC	Low-density parity-check
LS	Least square

LSTM	Long short-term memory
MAB	Multi-armed bandit
MBS	Macro BS
MIMO	Multiple-input multiple-output
ML	Machine learning
mmWave	Millimeter-wave communications
MU-MIMO	Multi-user multiple-input multiple-output
MWM	Maximum weighted matching
NI	National Instruments Corporation
NLOS	Non-line-of-sight
NN	Neural network
NOMA	non-orthogonal multiple access
NR	New radio
OFDM	Orthogonal frequency-division multiplexing
OFDMA	Orthogonal frequency division multiple access
ORA	Orthogonal resource allocation
OMA	Orthogonal multiple access
PBCH	Physical broadcast channel
PD-NOMA	Power-domain NOMA
PPP	Poisson point process
PRACH	Physical random-access channel
PSS	Primary synchronization sequence
QoS	Quality of Service
ReLU	Rectified linear units
RF	Radio frequency
RIS	Reconfigurable intelligent surface
RL	Reinforcement learning
RNN	Recurrent neural network
RSRP	Reference signal received power
SBS	Small BS
SCA	Successive convex approximation
SI	Self-interference
SIC	Successive interference cancellation
SINR	Signal-to-interference-plus-noise ratio
SISO	Single-input single-output
SL	Supervised learning
SNR	Signal to noise ratio
SRS	Sounding reference signal
SSB	Synchronization sequence blocks
SSS	Secondary synchronization sequence

SVM	Support vector machines
UCB	Upper confidence bound
UE	User equipment
UL	Uplink
ULA	Uniform linear array
UOA	National and Kapodistrian University of Athens
UPN	User provided network
V2X	Vehicle-to-everything
WP1	Work package 1

Table of Figures

Executive summary

This report includes the SEMANTIC ESR contributions towards the objectives of WP1 (Spectrum and Forward-Compatibility Aspects for multi-GHz NR operation).

More specifically, it summarizes the key findings and performance evaluation results of the ESRs in Task 1.3 Performance Evaluation and Experimentation. This task has been led by NI and contributing partners are CLM and UOA. ESRs contributing to this deliverable are CLM-1, CLM-2, NI-1, and UOA-1. This deliverable focuses on beam-based transmissions in multi-GHz bands; low-complexity techniques for channel estimation in massive MIMO in the millimeter-wave (mmWave) band; distributed MIMO with focus on Integrated access and backhaul (IAB); and non-orthogonal multiple access (NOMA) for enhancing user experience in beyond 5G systems.

The outcomes of this deliverable will be circulated to WP4 to convey to the respective ESRs a list of PHY components, resources and techniques towards the automated control and parameterization of the 3GPP 5G and Beyond (6G) NR evolution.

1 Introduction

In the quest to provide higher throughputs and to accommodate large number of mobile devices, 5G cellular communication technology has moved towards millimeter-wave (mmWave) bands with large bandwidths [RAP+13], [RRE14]. However, communication in these bands is subject to severe propagation loss, attenuation from atmospheric gases and precipitation, line-of-sight (LoS) blockage and scattering, and diffraction [MP05]. Beamforming with antenna arrays helps address these challenges [ROH14]. The small wavelength facilitates antenna arrays with large number of antennas at both base station (BS) and user equipment (UE). Large antenna arrays result in narrow beams with large array gains, which compensate for the severe propagation loss. However, narrow beams require accurate beam alignment [GPR+19]. To establish high directional links between BS and UE, 5G relies on a set of procedures known as beam management (BM). For initial access during BM, both BS and UE perform an exhaustive beam scan. However, large size codebooks at higher frequencies complicate the exhaustive beam scan-based BM resulting in large beam measurement overhead and consequently reduced spectral efficiency. Machine learning (ML) is very well known to deal with complex problems in computer vision and more recently in wireless communications. Consequently, several studies propose the use of ML for mmWave BM [KGP+23]. Thus, in the following chapters, we propose our solution for the ML-based mmWave BM and compare it with the state of the art.

mmWave MIMO is now a reality with great potential for further improvement. We study full-duplex transmissions as an effective way to improve mmWave MIMO systems. Compared to half-duplex systems, full-duplex transmissions may offer significantly higher data rates and lower latency. However, full-duplex transmission is hindered by self-interference (SI) at the receive antennas and SI channel estimation becomes a crucial step to make full-duplex systems feasible. Already, there are several challenges in channel estimation of mmWave MIMO systems, such as high pilot overhead, pilot contamination, etc. With the additional need for SI channel estimation, utilizing full-duplex transmissions will further complicate the channel estimation bottleneck in full-duplex mmWave MIMO systems. In this work, we address the problem of channel estimation in full-duplex mmWave MIMO systems using neural networks (NNs). Our approach involves sharing pilot resources between users and transmit antennas at the BS, aiming to reduce the pilot overhead in full-duplex systems and achieve a comparable overhead to that of a half-duplex system. Simulation results demonstrate the superiority of the NN-based approach over the conventional minimum mean squared error (MMSE) channel estimator. We conduct various experiments to understand how NNs perform the estimation with different architectures, (e.g., different numbers of hidden layers), the introduction of non-linear distortion (e.g., with 1-bit ADCs), and different channel conditions (e.g., low-correlated and high-correlated channels). Our simulations provide novel insights into NN-based channel estimators. Additionally, in the case of separate antenna configurations in full-duplex systems, obtaining channel estimates of transmit antenna arrays to the downlink UEs poses another challenge. To address this, we propose estimating both uplink and downlink UEs at the receive chain and then employing a NN to map the channel from receive antenna arrays to downlink UEs and transmit antenna arrays.

Non-orthogonal multiple access (NOMA) has become a promising technology for next-generation wireless communications systems due to its capability to provide access for multiple users on the same resource. In this work, we consider an uplink power-domain NOMA system aided by a reconfigurable intelligent surface (RIS) in the presence of a jammer that aims to maximize its interference on the BS uplink receiver. We consider two kinds of RISs, a regular RIS whose elements can only change the phase of the incoming wave, and an RIS whose elements can also attenuate the incoming wave. Our aim is to minimize the total power transmitted by the user terminals under quality-of-service constraints by controlling both the propagation from the users and the jammer to the BS with the help of the RIS. The resulting objective function and constraints are both non-linear and non-convex, so we address this problem using numerical optimization. Our numerical results show that the RIS can help to dramatically reduce the per-user required transmit power in an interference-limited scenario.

Integrated Access and Backhaul (IAB) is an emerging technology that has gained significant attention from both industry and academia in recent years. As wireless networks evolve towards 5G and beyond, providing reliable backhaul connections to base stations is becoming increasingly challenging due to high costs and limitations of wired fiber deployment [MMF+20]. The 3rd Generation Partnership Project (3GPP) identified IAB as a promising solution that can enable flexible deployment of wireless backhaul using existing radio resources [3GP+20]. In the IAB architecture specified by 3GPP, certain base stations called IAB-nodes establish wireless backhaul links to relay traffic between user equipment and the core network via parent nodes [3GP+20]. This creates a multi-hop wireless backhaul or fronthaul mesh that eliminates the need for dedicated wired infrastructure between every base station [SAD18]. 3GPP introduced integrated access and backhaul where the same spectrum is reused for access and backhaul transmissions [SD19]. Several field trials have demonstrated the technical feasibility of IAB networks. However, key challenges remain around interference management, mobility support, integration with existing systems and development of efficient IAB-specific protocols [SD19], [LWS20]. Resource allocation in IAB networks poses unique challenges compared to traditional cellular deployments due to the tight integration of access and backhaul. 3GPP has specified that radio resources in IAB need to be dynamically shared between access and backhaul transmissions [3GP+20]. As IAB deployments become more complex with increasing backhaul hops, efficient distributed resource management strategies that can scale are crucial to unlock the full potential of shared access-backhaul networks.

2 Background on Relevant Technologies

2.1 Machine Learning-based mmWave Beam Management

The wireless communication at higher frequency bands (mmWave and THz bands) suffers from higher propagation loss and severe channel intermittency. To compensate these impairments, beamforming with highly directional transmission links achieved via high dimensional phased antenna arrays is used at the BS and the UE [RPM+21]. Consequently, a precise alignment of beams is required for link establishment. Beam alignment in 5G is achieved through a set of operations known as BM [GPR+19]. The BM procedure specified by 3GPP for 5G NR includes initial beam establishment, beam refinement and tracking, and beam failure detection and recovery [GPR+19]. However, the BM procedure specified by 3GPP suffers from higher beam measurement overhead, increased latency, and higher power consumption. In deliverable 1.2, we have provided a detailed overview of BM procedure along with its limitations.

Inspired by the successful application of ML in natural language processing and computer vision, ML has also been harnessed in wireless communications [HCN+21, KKI+21]. Compared to traditional mathematical modeling-based methods, ML based models have several key advantages. Firstly, traditional mathematical models usually rely on idealized assumptions and may not represent the system accurately. ML models, on the other hand, can model the system's non-linearity and thus can represent it perfectly. Secondly, ML models are highly capable of capturing the high-dimensional features of the propagation environment, such as mobility patterns and blockage locations. Based on these motivations, ML has widely been researched for several aspects of wireless communications including beam management [AHS+22, DA22]. In deliverable 1.2, we have provided a comprehensive overview of ML-based BM approaches. The outcome of our literature review has been published in [KGP+23]. The survey paper classifies the existing ML-based BM approaches in supervised, reinforced, and federated learning and sub-divides these approaches based on the architecture of the neural network. Figure 1, taken from our publication, presents a summary of discussed ML-based BM approaches [KGP+23].

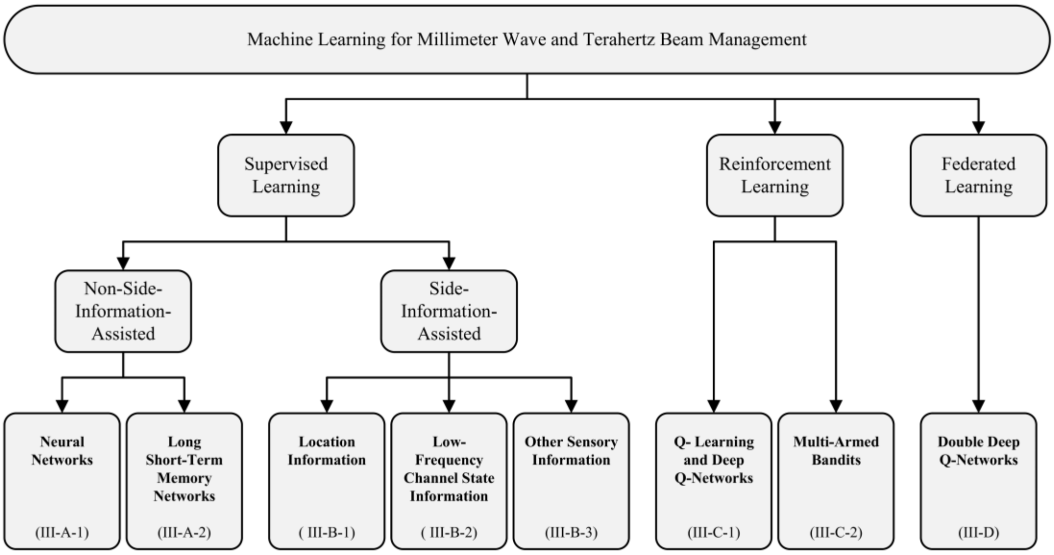

Figure 1: Classification of ML-based beam management solutions for mmWave and terahertz bands presented in [KGP+23].

2.2 Full-duplex mmWave Massive MIMO Channel Estimation

Current key enabling wireless technologies, such as massive multiple-input-multi-output (MIMO), mmWave communication, ultra-dense networks, etc., have significantly improved the throughput of wireless communication [BH+14]. mmWave communication can meet high data rate demands thanks to the huge bandwidth available in this band, and the high path loss in these frequencies can be compensated by utilizing the beamforming gain of massive MIMO antennas.

Nonetheless, these technologies have mainly been studied for half-duplex communication, and the potential of utilizing full-duplex communication has been overlooked. In full-duplex transmission, a transceiver can simultaneously transmit and receive over the same frequency carrier, thus possibly doubling the spectral efficiency compared to half-duplex systems. Besides, the delay associated with half-duplex transmission would be alleviated in full-duplex systems, facilitating meeting low latency requirements for 5G and beyond [SS+14], [RA+21].

To realize the full-duplex transmission, the self-interference (SI), which is caused by each transmit element onto the entire receive array, has to be canceled out. Three steps are usually considered for mitigating the SI channel effect at the receive antenna arrays: propagation, analog, and digital domain cancellations. In the propagation domain cancellation, SI power is suppressed before reaching the receive chain circuits, while analog domain cancellation is performed before the analog-to-digital converter (ADC) in the receive analog chain. Finally, digital domain cancellation suppresses residual SI power remaining from the propagation and analog domains.

There are two main antenna configurations used for full-duplex systems: separate antenna full-duplex and shared antenna full-duplex. Separate antenna full-duplex systems use separate antennas for transmission and reception, providing high isolation and low interference. On the other hand, shared antenna full-duplex systems use a single antenna for both functions, offering a simpler design and lower hardware costs [SS+14], [ES+14].

2.3 Non-orthogonal Multiple Access

2.3.1 Literature on Non-orthogonal Multiple Access (NOMA)

NOMA is an interesting technique since it enables multiple access of many users in the same resource and is generally divided into two main classes: power-domain and code-domain [SZS+18]. Power-domain NOMA (PD-NOMA) exploits situations where the users have different power levels. As Figure 2 illustrates, in the downlink of power-domain NOMA, the users nearer to the BS have better channel conditions compared to distant users who require higher transmission power to mitigate the higher path loss. The idea behind power-domain NOMA is that the users nearer the BS can employ successive interference cancelation (SIC) to remove the strong signal destined to the remote users before decoding their own signal [TJ91].

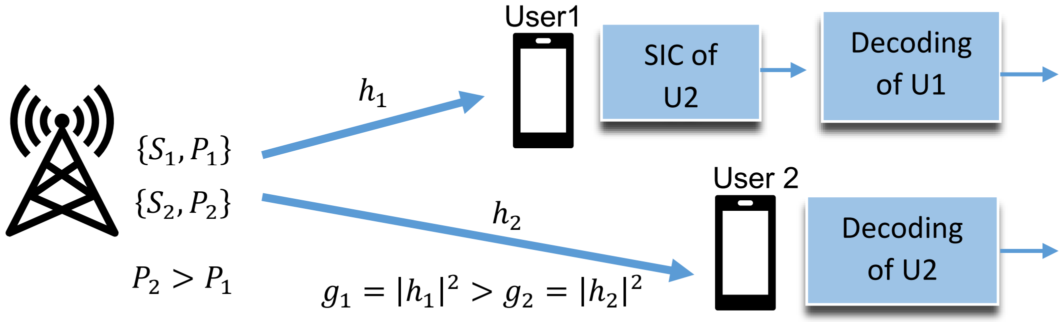

Figure 2: Illustration of Downlink of Power-domain NOMA.

In the uplink power-domain NOMA, as Figure 3 illustrates, the SIC is implemented at the receiver of the BS. In the first step, the receiver decodes the signal of the near user that has a better channel condition, it subtracts it from the received signal to decode the signal of the far user [YYA+13].

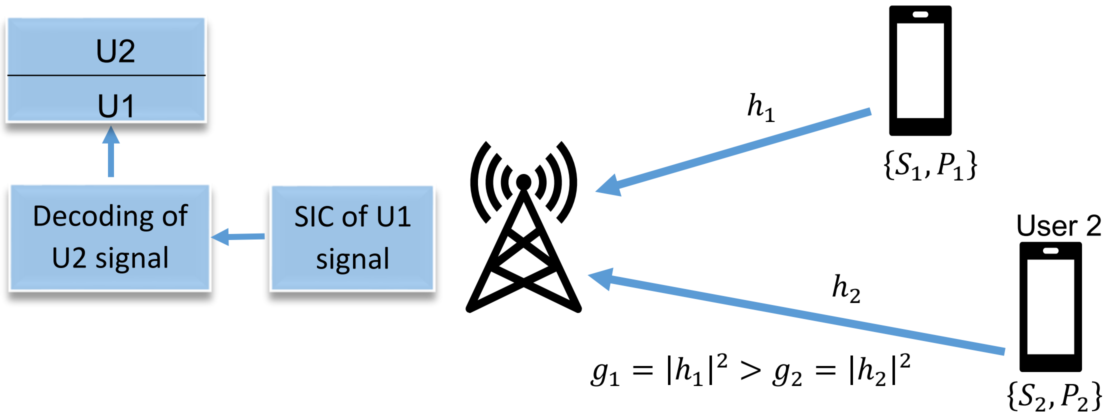

Figure 3: Illustration of Uplink of Power-domain NOMA.

The superiority of NOMA over conventional orthogonal multiple access (OMA) techniques is derived from the improved spectral efficiency due to the sharing of time/frequency/space/code resources, its allocation of different Quality of Service (QoS) levels to users based on power level allocation, and the fact that it supports massive connectivity, lower latency, and an enhanced cell-edge user experience [IZD17].

2.3.2 Literature on Reconfigurable Intelligent Surface (RIS)

An RIS is a surface consisting of electromagnetic material. The surface usually consists of a large number of low-cost reflecting elements whose properties can be controlled. In a conventional RIS design, the phase of the reflection coefficient of each element is controlled to enable modification of the propagated waves [XYS+21]. More recently, RIS designs have been proposed to enable control of both the phase and the attenuation of each element, providing additional degrees of freedom for shaping the resulting wave field [XRC22], [IM22]. RIS technology has been proposed for many different types of wireless communication scenarios, including NOMA [YXY+21], [XYS+21]. It has been shown that the performance of NOMA systems can be improved by increasing the number of reflecting elements [LDT+21], and the spectral efficiency can be significantly enhanced with RIS-assisted NOMA, compared to NOMA without RIS and traditional OMA [YXY+21].

The use of RIS has emerged as a unique technology for improving both spectral and energy efficiency. An RIS consists of an array of elements whose reflective properties can be individually controlled, enabling some degree of control of the wireless propagation environment [LLM+21]. In a conventional RIS implementation, it is the phase shift of the reflection coefficient of each element that is adjusted in order to achieve the desired effect on the wireless channels.

More recently, researchers have also studied RIS architectures where both the phase shift and the attenuation of the reflection coefficient of each element can be individually controlled, so-called absorptive RIS (A-RIS). In our work, the energy absorbed by the A-RIS can be refracted to directions on the other side of the surface [YXJ+21], [SHB+22] or sampled using an active radio frequency (RF) receiver for channel estimation or sensing [XRC+22], [ADS+22]. RIS technology has been applied in many different types of wireless communications scenarios, including NOMA [YXY+21]. However, while the use of conventional phase-shift-only RIS has been proposed for NOMA applications with the goal of improving spectral efficiency, to our knowledge there is no work reported on using A-RIS with NOMA, nor on using RIS to mitigate the impact of external interference (e.g., jamming) on NOMA performance.

2.4 Integrated Backhaul and Access

The IAB is a new feature in 5G networks that extends coverage by efficiently using the spectrum traditionally reserved for access. However, meeting the stringent ultra-reliability and low latency (URLLC) requirements for advanced 5G services presents challenges for the multi-hop network design of IAB. To address this, the authors in [YRC22] have suggested a cross-layer design for routing and resource allocation under the current 3GPP 5G standards. They create a routing problem that minimizes latency while maintaining reliability, followed by a reinforcement learning framework to solve the resource allocation and routing problem based on local information of each IAB node. They propose an entropy-based Reinforcement learning (RL) algorithm with a federated learning mechanism to enhance performance and speed up convergence. The available resources in IAB networks must be carefully tuned in a complex setting that includes directional transmissions, device heterogeneity, and intermittent links with varying levels of availability that changes rapidly over time. The authors in [ZDF+21] introduced a new approach. They believe that the traditional optimization techniques may not be sufficient to provide the best performance in these conditions. Therefore, a Deep Reinforcement Learning (DRL) framework assisted with Long Short-Term Memory (LSTM) has been proposed to implicitly learn the best resource allocation strategy in networks affected by obstacle blockages. The introduced framework is based on Column Generation (CG) and demonstrates remarkable effectiveness in addressing routing and link scheduling in mmWave 5G IAB networks in realistic scenarios.

A flexible and low-complexity semi-centralized resource allocation scheme has been proposed for IAB networks in [PZP+22], which adheres to the 3GPP IAB specifications. The solution involves a version of the Maximum Weighted Matching (MWM) problem that operates on a spanning tree representing the IAB network, with a complexity that is linear in the number of IAB-nodes. To assess its effectiveness, the proposed approach is compared against existing distributed methods using end-to-end, full-stack system-level simulations employing a 3GPP-compliant channel model, protocol stack, and various user applications.

The presented work in [SM23] has been examined a millimeter-wave network that is dynamic and has integrated access and backhaul, where mobile relay nodes move to self-configure the wireless backhaul. The focus was on in-band relaying networks, which operate access and backhaul links on the same frequency band, with strict constraints on co-channel interference. In this scenario, the authors jointly investigated the intricate problem of dynamic relay node positioning, user association, and backhaul capacity allocation. To tackle this problem with limited complexity, they employ a hierarchical multi-agent reinforcement learning approach with a two-level structure. A high-level policy dynamically coordinates mobile relay nodes and defines the backhaul configuration for a low-level policy that jointly assigns user equipment to each relay and allocates backhaul capacity accordingly. The resulting solution automatically adjusts the access and backhaul network based on changes in the number of users, traffic distribution, and channel variations.

The authors in [AH22] present a distributed stochastic approach that simultaneously tackles the problems of resource/bandwidth allocation and path selection in a multi-hop multi-path IAB mm-wave 5G network. They first propose a Directed Acyclic Graph (DAG) topology formation algorithm that performs cell search and initial access procedures and disseminates topology information across child/parent links. Next, they employ stochastic optimization tools to select paths from a resource perspective and investigate the efficiency of the proposed scheme in resource utilization. They also analyze the impact of stochastic information spread in the topology and probability levels on the performance of the scheme. The findings demonstrate that the proposed distributed scheme achieves performance like that of an optimal centralized algorithm in joint resource allocation and path selection tasks, making it a potential alternative to centralized resource management in scenarios where central resource allocation is not feasible.

Looking at some of the previous works on the topic of IAB, we find that most of the works defined an optimization problem to reach a specific goal. Due to the difficulty of solving the problem with respect to the time complexity, tools such as reinforcement learning, stochastic optimization and Heuristic algorithms have been proposed. Table 1 shows a brief comparison between some important works that have been presented in the literature.

Table 1: Comparison between different works in IAB technology.

	Goal	**Modelling tool**	**Structure**
[YRC22]	Minimizes latency	Entropy-based algorithm with Reinforcement learning	Centralized
[ZDF+21]	Maximize the number of bits in a frame sent	Mixed-integer linear programming (MILP) - Deep Reinforcement Learning (DRL)	Centralized
[PZP+22]	Maximum Weighted Matching (MWM) problem	Heuristic algorithm to find (minimum spanning tree) MSP	Centralized
[SM23]	Problem of dynamic relay node positioning, user association, and backhaul capacity allocation	a hierarchical multi-agent reinforcement learning	Centralized
[AH22]	Resource/bandwidth allocation and path selection	stochastic optimization	Distributed

3 Algorithmic Framework

3.1 Machine Learning-based mmWave Beam Prediction

In this section, we describe the system model and algorithmic framework of our proposed ML based mmWave beam prediction approach.

3.1.1 System Model

3.1.1.1 Channel Model

We consider the downlink mmWave multiple-input multiple-output (MIMO) communication system serving a single user, where BS and UE are equipped with M_{TX} and M_{RX} antennas, respectively. Further, assume that a single radio frequency (RF) chain is employed at both BS and UE sides. We assume the three-dimensional (3D) channel model, where azimuth and elevation angles are considered. We consider the clustered channel model with C clusters with L_c per cluster. Specifically, the channel matrix $\mathbf{H} \in C^{M_{RX} \times M_{TX}}$ can be expressed as [3GP+22]

$$\mathbf{H} = \sqrt{\frac{M_{TX} M_{RX}}{\rho_{LOS}}} \alpha_{\mathrm{LOS}} \mathbf{a}_{\mathrm{R}}(\phi_{\mathrm{LOS}}^{\mathrm{R}}, \theta_{\mathrm{LOS}}^{\mathrm{R}}) \mathbf{a}_{\mathrm{T}}^{H}(\phi_{\mathrm{LOS}}^{\mathrm{T}}, \theta_{\mathrm{LOS}}^{\mathrm{T}}) + \sum_{c=1}^{C} \sqrt{\frac{M_{TX} M_{RX}}{\rho_c}} \sum_{l=1}^{L_c} \alpha_{c,l} \mathbf{a}_{\mathrm{R}}\left(\phi_{c,l}^{\mathrm{R}}, \theta_{c,l}^{\mathrm{R}}\right) \mathbf{a}_{\mathrm{T}}^{H}\left(\phi_{c,l}^{\mathrm{T}}, \theta_{c,l}^{\mathrm{T}}\right) . \qquad (3.1)$$

In this model, the c-th cluster containing L_c paths has a pathloss ρ_c, azimuth and elevation angle-of-arrival (AoA) ϕ_c^R, θ_c^R , respectively, and azimuth and elevation angle-of-departure (AoD) ϕ_c^T, θ_c^T, respectively, while α_c is the complex gain corresponding to the l-th path in the c-th cluster. Similar notations are used for the LOS path. Furthermore, $\boldsymbol{a}_T \in C^{M_{TX} \times 1}$ and $\boldsymbol{a}_R \in C^{M_{RX} \times 1}$denote the antenna response vectors of BS and UE, respectively. We assume a uniform planar array with the following response.

$$\mathbf{a}(\phi, \theta) = \frac{1}{\sqrt{N}} [1, \cdots, e^{j \frac{2\pi}{\lambda} d\left(y' \sin(\phi) \sin(\theta) + z' \cos(\theta)\right)}, \cdots, e^{j \frac{2\pi}{\lambda} d\left(\left(N_y - 1\right) \sin(\phi) \sin(\theta) + \left(N_z - 1\right) \cos(\theta)\right)}]^T \qquad (3.2)$$

Here, y' and z' indicate the antenna element number while λ and d indicate the wavelength and the antenna element spacing.

3.1.1.2 Beam Training Model

We assume that phase shifter based analog beamforming is applied, where $\mathbf{f} \in C^{M_{TX}\times 1}$ is denoted as the transmitting beam of BS, and $\mathbf{w} \in C^{M_{RX}\times 1}$ is denoted as the receiving beam of UE. The transmitting and receiving beams are selected from the predefined codebooks $\boldsymbol{F}$ and $\boldsymbol{W}$, which consist of N_{TX} and N_{RX} candidate beams, respectively. The candidate transmitting beam $\boldsymbol{f}_m, m\ \{1,2,\ldots,N_{TX}\}$, and receiving beam $\boldsymbol{w}_n, n\ \{1,2,\ldots,N_{RX}\}$, can be written respectively as

$$\mathbf{f} = \left\{\mathbf{a}_{\mathrm{T}}\left(\overline{\phi}_1^{\mathrm{T}}, \overline{\theta}_1^{\mathrm{T}}\right), \mathbf{a}_{\mathrm{T}}\left(\overline{\phi}_2^{\mathrm{T}}, \overline{\theta}_2^{\mathrm{T}}\right), \cdots, \mathbf{a}_{\mathrm{T}}\left(\overline{\phi}_{TX}^{\mathrm{T}}, \overline{\theta}_{TX}^{\mathrm{T}}\right)\right\},$$

$$\mathbf{w} = \{\mathbf{a}_{\mathrm{R}}(\overline{\phi}_1^{\mathrm{R}}, \overline{\theta}_1^{\mathrm{R}}), \mathbf{a}_{\mathrm{R}}(\overline{\phi}_2^{\mathrm{R}}, \overline{\theta}_2^{\mathrm{R}}), \cdots, \mathbf{a}_{\mathrm{R}}(\overline{\phi}_{RX}^{\mathrm{R}}, \overline{\theta}_{RX}^{\mathrm{R}})\}. \tag{3.3}$$

Here $\overline{\phi}_1^{\mathrm{T}} (\overline{\theta}_1^{\mathrm{T}})$ and $\overline{\phi}_1^{\mathrm{R}} (\overline{\theta}_1^{\mathrm{R}})$ indicate the azimuth (elevation) direction for transmit and receive beam, respectively. Given the channel matrix $\boldsymbol{H}$ and beam pair $\{\boldsymbol{f}, \boldsymbol{w}\}$, the received signal y can be written as

$$y = \sqrt{P}\mathbf{w}^H \mathbf{H}\mathbf{f}x + \mathbf{w}^H \boldsymbol{\eta} \tag{3.4}$$

where P is the transmit power and x is the transmitted signal, while $\boldsymbol{\eta} \in C^{M_{RX}\times 1}$ denotes the additive white Gaussian noise (AWGN).

Beam training aims to find the optimal beam pair $\{\boldsymbol{f}_{m^*}, \boldsymbol{w}_{n^*}\}$ with the maximum beamforming gain, which can be formulated as the following optimization problem:

$$\{m^*, n^*\} = \underset{\substack{m\in\{1,2,\cdots,N_{TX}\},\\ n\in\{1,2,\cdots,N_{RX}\}}}{\operatorname{argmax}} |\boldsymbol{w}_n^H \boldsymbol{H} \boldsymbol{f}_m|^2. \tag{3.5}$$

A straightforward scheme of beam training to solve the above optimization is the brute-force beam search, where all the candidate transmitting and receiving beams are swept to find the beam pair with the maximum power of the received signal. However, this scheme requires $N_{TX}N_{RX}$ measurements, which leads to excessively huge training overhead. To tackle this problem, the two-level beam search based on a hierarchical multi-resolution codebook can be considered, where the codebook consists of the wide beam codewords in the first level and the narrow beam codewords in the second level. Based on the hierarchical multi-resolution codebook, the beam search is divided into two levels. The first-level searches for coarse beam alignment based on the wide beam codebook, given by:

$$\{m_{\mathrm{w}}^*, n_{\mathrm{w}}^*\} = \underset{\substack{m_{\mathrm{w}}\in\{1,2,\cdots,N_{TX}/s_{TX}\},\\ n_{\mathrm{w}}\in\{1,2,\cdots,N_{RX}/s_{RX}\}}}{\operatorname{argmax}} |\boldsymbol{w}_{w,n}^H \boldsymbol{H} \boldsymbol{f}_{w,m}|^2. \tag{3.6}$$

Here, $\boldsymbol{f}_w$ and $\boldsymbol{w}_w$ indicate the beamforming vector corresponding to wider transmit and receive beam, respectively. The first level search requires $N_{TX}N_{RX}/s_{TX}s_{RX}$ measurements, where s_{TX} *defines the number of* narrow beams within each wide beam. The second-level search confirms the 'optimal' narrow beam pair in the range of the selected wide beam pair, given by:

$$\{m^*, n^*\} = \underset{\substack{m\in\{(m_{\mathrm{w}}^*-1)s_{\mathrm{TX}}+1,\cdots,m_{\mathrm{w}}^* s_{\mathrm{TX}}\},\\ n\in\{(n_{\mathrm{w}}^*-1)s_{\mathrm{RX}}+1,\cdots,n_{\mathrm{w}}^* s_{\mathrm{RX}}\}}}{\operatorname{argmax}} |\boldsymbol{w}_{w,n}^H \boldsymbol{H} \boldsymbol{f}_{w,m}|^2. \tag{3.7}$$

The second-level search needs further $s_{TX}s_{RX}$ measurements. Hence, the two-level beam search requires $\frac{N_{TX}N_{RX}}{s_{TX}s_{RX}} + s_{TX}s_{RX}$ measurements, which is significantly smaller than that imposed by the brute-force beam search. Another overhead-reducing scheme is the interactive beam search, which selects the beams at BS and UE sides separately. Specifically, with UE antennas set to be the omni-directional pattern, BS sweeps all candidate transmitting beams to find the one with the maximum beamforming gain. Then with this 'optimal' transmitting beam, UE sweeps all candidate receiving beams to find the beam with the maximum beamforming gain. In other words, the 'optimal' beam pair are obtained by solving the following two optimization problems separately:

$$m^* = \underset{m\in\{1,2,\cdots,N_{TX}\}}{\operatorname{argmax}} |\boldsymbol{H}\boldsymbol{f}_m|^2,$$

$$n^* = \underset{n\in\{1,2,\cdots,N_{RX}\}}{\operatorname{argmax}} |\boldsymbol{w}_n^H \boldsymbol{H}\boldsymbol{f}_{m^*}|^2. \tag{3.8}$$

This scheme requires $N_{TX} + N_{RX}$ measurements, which is much lower than the brute-force search.

3.1.2 A Low-Complexity Machine Learning Design for mmWave Beam Prediction

As indicated above, the beam search can be implemented at BS and UE separately. For simplicity, we investigate the selection of the transmitting beams at BS side, where the UE beam is assumed to be ideal.

3.1.2.1 Problem Formulation and Algorithmic Framework

To reduce the beam training overhead, we propose to train a small number of candidate beams and calibrate the beam direction according to the received signals [HM+19]. How to find properly trained beams that achieve high accuracy under the given training overhead is crucial. Motivated by the two-level beam search with low training overhead where the wide beam codebook can cover the whole angular space, we propose to measure the reference signal received power (RSRP) of wide beams for calibrating the beam direction [CRJ19]. Additionally, as wider, and narrow beams cover the same angular direction, there exists a spatial correlation between wide and narrow beams as shown in Figure 4 [NKD15]. For convenience, we define the received signal of the m-th candidate wide beam as $y_{w,m}$ and its RSRP as $RSRP_{w,m}$. Since the narrow beam codebook enjoys higher angular resolution, the proposed calibrated beam training scheme aims to predict the index of the optimal narrow beam at BS side m^* based on the received signal RSRP. Because the number of candidate narrow beams is limited, the prediction can be formulated as a multi-classification task, where each classified category corresponds to one candidate narrow beam. Mathematically, the prediction model can be represented by the classification function $f1(\cdot)$ as

$$m^* = f1(RSRP_w), \qquad m^* \ \{1, 2, \ldots, N_{TX}\} \tag{3.9}$$

However, it is difficult to implement this prediction by conventional estimation methods due to the non-linear relation between channel directivity and received RSRP. Consequently, deep learning with strong ability to learn complex nonlinear relations is utilized to implement the prediction.

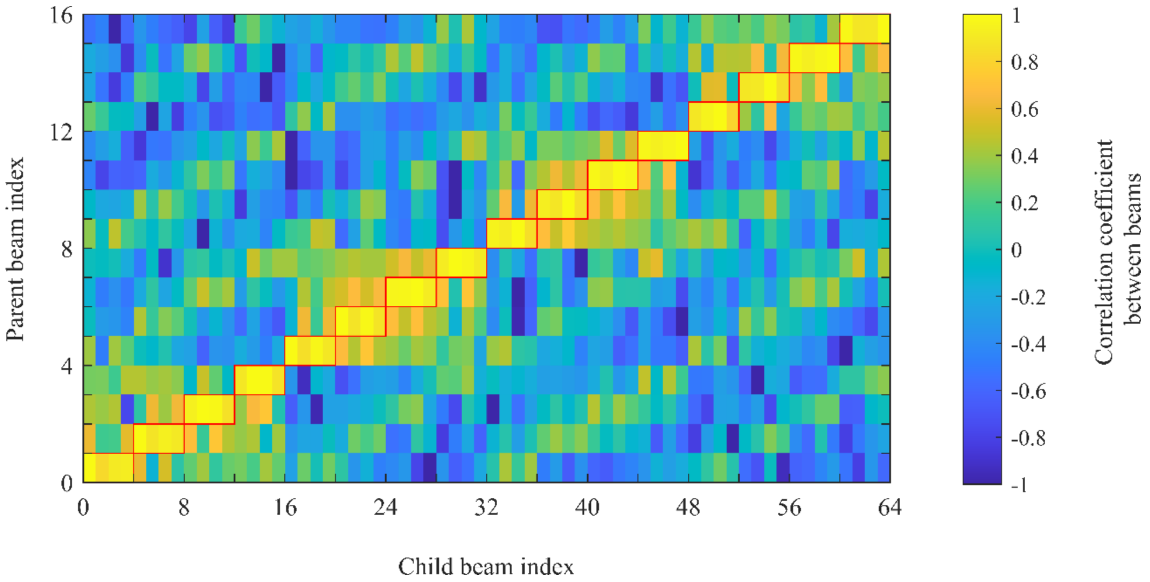

Figure 4: Spatial angular correlation between wide and narrow beams.

3.1.2.2 Proposed Machine Learning Model Design for mmWave Beam Prediction

In this section, we provide details of our ML model design and its corresponding inputs and outputs. Our proposed scheme consists of three stages: training, validation, and inference. In the training stage, training data are collected to train the deep learning model, where each sample comprises a RSRP vector as the model input and the index of the corresponding optimal narrow beam as the classification label, which can be obtained by conventional beam training schemes and fed back to BS. In the validation phase, the parameters of the ML model are fine tuned. After the model is well-trained and well-validated with sufficient data, it switches to the inference stage. In this stage, BS only perform the wide beam search, and the corresponding received signals are leveraged to predict the optimal narrow beam by the well-trained model as shown in Figure 5. Thus, the narrow beam search is avoided, and the overhead of beam training is reduced considerably.

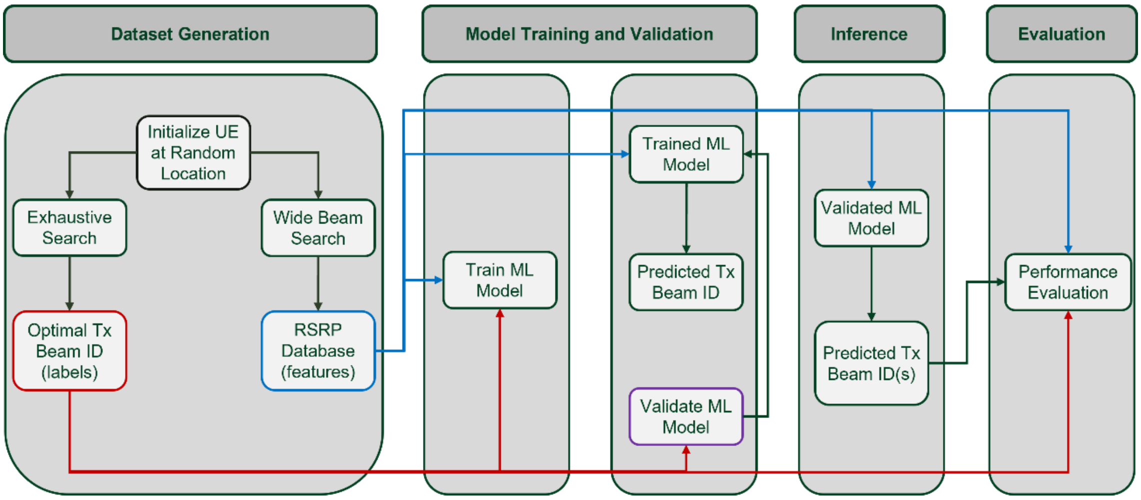

Figure 5: Machine learning model training, validation, and inference.

Artificial neural network (ANN) is adopted to implement the prediction due to its outstanding performance in classification tasks. The proposed ANN based model is depicted in Figure 6. The proposed model consists of input, output, and a SoftMax layer. The input layer of our proposed network consists of $\frac{N_{TX}}{S_{TX}}$ nodes and takes RSRP values of the wider beams as its input. The output layer consists of N_{TX} nodes. Finally, a softmax layer is introduced, which returns the probability of each narrower beam being the best. Finally, the narrow beam with the maximum predicted probability is selected, i.e.,

$$\hat{m}^* = \underset{m\in\{1,2,\cdots,N_{TX}\}}{\operatorname{argmax}} \hat{\mathcal{P}}_m. \qquad (3.10)$$

The predicted probabilities provide the qualities of beams, and a beam with larger probability is predicted to enjoy higher beamforming gain over other beams with smaller probabilities. Further, we consider mean squared error as the loss function and the model is trained via Adam optimizer.

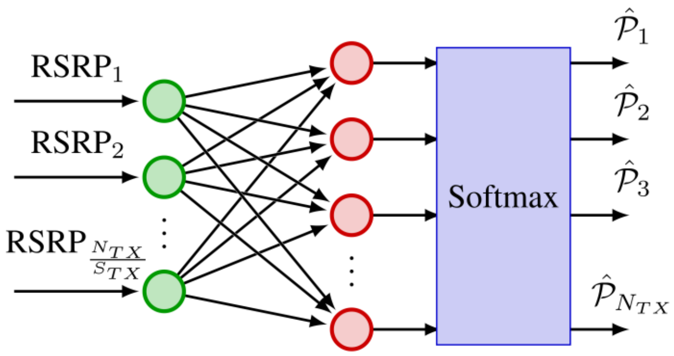

Figure 6: Proposed low-complexity design for ML-based mmWave beam prediction.

3.2 SI and UE Channel Estimation

To estimate the channels of UEs and SI, both downlink and uplink UEs, along with transmit antennas at the BS, transmit pilot signals to the receive antenna at the BS. We assume that the received SI signal power remains stronger than the received UE signal power, even after SI cancellation in the propagation domain. Hence, our approach involves initially estimating the SI channel and subsequently subtracting the estimated SI signal from the received pilot signal to estimate the UE channel.

The received pilot signal at receive antenna arrays for SI channel estimation will be:

$$\mathbf{Y_{SI}} = \sqrt{SNR_{SI}}\mathbf{H_{SI}FX_{SI}} + \sqrt{SNR_{UE}}\mathbf{H_{UE}X_{UE}} + \mathbf{N}, \qquad (3.11)$$

where $\mathbf{Y_{SI}} \in \mathbb{C}^{N_r \times \tau}$ is the received pilot signal at receive antennas of BS during τ pilot transmissions. $\mathbf{X_{UE}} \in \mathbb{C}^{K \times \tau}$ is the transmitted pilot signal from K UEs, $\mathbf{X_{SI}} \in \mathbb{C}^{\tau \times \tau}$ is a diagonal matrix whose diagonal elements are transmitted pilot signals from transmit antennas at BS, $\mathbf{F} \in \mathbb{C}^{N_t \times \tau}$ is the precoding matrix of transmit antennas of BS, and $\mathbf{H_{UE}} = [\mathbf{h_1^{(u)}}, \mathbf{h_2^{(u)}}, \dots, \mathbf{h_{K_u}^{(u)}}, \mathbf{h_1^{(d)}}, \mathbf{h_2^{(d)}}, \dots, \mathbf{h_{K_d}^{(d)}}] \in \mathbb{C}^{N_r \times K}$ is concatenated uplink and downlink channels, where k-th column is the channel of k-th uplink or downlink UE to the receive antenna at BS. We assume all UEs have the same transmit power denoted by $\mathrm{p_{UE}}$ and $\mathrm{p_{SI}}$ is the transmit power from transmit antenna arrays. SNR_{SI} and SNR_{UE} are defined as

$$SNR_{SI} = \frac{p_{SI}}{\sigma_n^2}$$

$$SNR_{UE} = \frac{p_{UE}}{\sigma_n^2}, \qquad (3.12)$$

where σ_n^2 is the noise variance. The matrix $\mathbf{N} \in \mathbb{C}^{N_r \times \tau}$ is additive noise which is comprised of independent and identically distributed (i.i.d.) elements following a zero-mean unit variance Gaussian distribution. Note that for the pilot dimension is $\tau = N_t + K$, the received pilot signal for SI channel estimation will be:

$$\mathbf{Y}_{\mathbf{SI}} = \sqrt{SNR_{SI}}\mathbf{H}_{\mathbf{SI}}\mathbf{F}\mathbf{X}_{\mathbf{SI}} + \mathbf{N},\ \tau = 1,2,\dots,N_t. \tag{3.13}$$

We apply the orthogonal pilot code book for both precoded SI signal from transmit antenna arrays and UEs during pilot transmission. Specifically, we utilize the discrete Fourier transform (DFT) pilot codebook, e.g., $\mathbf{F}\mathbf{X}_{\mathbf{SI}} = \mathbf{W}_{N_t\times\tau}, \mathbf{X}_{\mathbf{UE}} = \mathbf{W}_{K\times\tau}$, where,

$$\mathbf{W}_{N\times M} = \frac{1}{\sqrt{N}}\begin{bmatrix} 1 & 1 & 1 & \cdots & 1 \\ 1 & \omega & \omega^2 & \cdots & \omega^{M-1} \\ 1 & \omega^2 & \omega^4 & \cdots & \omega^{2(M-1)} \\ 1 & \omega^3 & \omega^6 & \cdots & \omega^{3(M-1)} \\ \vdots & \vdots & \vdots & \ddots & \vdots \\ 1 & \omega^{N-1} & \omega^{2(N-1)} & \cdots & \omega^{(N-1)(M-1)} \end{bmatrix} \tag{3.14}$$

where $\omega = e^{-2\pi j/M}$. We assume that SI is sufficiently canceled out in the propagation domain and the received signal at the baseband does not exceed the dynamic range of ADCs. We refer to the propagation domain SI cancelation before the digital domain as ϵ_{SI}, therefore, we re-write the SI channel as:

$$\mathbf{H}_{\mathbf{SI}} = \sqrt{\epsilon_{SI}}\sqrt{\frac{\kappa}{\kappa+1}}\mathbf{H}_{\mathbf{SI,NF}} + \sqrt{\frac{1}{\kappa+1}}\mathbf{H}_{\mathbf{SI,FF}}. \tag{3.15}$$

Note that the SI cancelation in the propagation domain can only suppress the near field channel from the transmit antenna arrays to the receive antenna arrays. In the digital domain after acquiring the estimate of the SI channel, the residual near-field and far-field SI channels can be further suppressed.

After SI channel estimation, we use the estimated SI channel to cancel out the SI signal power from the received pilot signal to estimate the UE channel. Therefore, the received pilot signal for UE channel estimation will become:

$$\mathbf{Y}_{\mathbf{UE}} = \sqrt{SNR_{UE}}\mathbf{H}_{\mathbf{UE}}\mathbf{X}_{\mathbf{UE}} + \sqrt{SNR_{SI}}\mathbf{E}_{\mathbf{SI}}\mathbf{F}\mathbf{X}_{\mathbf{SI}} + \mathbf{N}, \tag{3.16}$$

where $\mathbf{E}_{\mathbf{SI}} = \mathbf{H}_{\mathbf{SI}} - \widehat{\mathbf{H}}_{\mathbf{SI}}$ is the SI cancelation error, and $\widehat{\mathbf{H}}_{\mathbf{SI}}$ is the estimated SI channel.

For the pilot dimension $\tau = N_t + K$, the received pilot signal does not contain the signal from SI channel, thus,

$$\mathbf{Y}_{\mathbf{UE}} = \sqrt{SNR_{UE}}\mathbf{H}_{\mathbf{UE}}\mathbf{X}_{\mathbf{UE}} + \mathbf{N},\ \tau = 1,2,\dots,K \tag{3.17}$$

Typically, the channel of nearby UEs is correlated, and for the pilot dimension $\tau = N_t$ and $\tau = K$, the residual error from SI cancellation introduces further correlation in the received pilot signals used for UE channel estimation. Therefore, we estimate the entire UE channel matrix, denoted as $\mathbf{H_{UE}}$, to take advantage of the correlation resulting from imperfect SI cancellation. This allows us to leverage the additional information for a more accurate estimation of the UE channels.

3.2.1 LS, MMSE, NN-based Channel Estimation

In this section, we present three channel estimation methods: LS, MMSE, and NN-based estimators for both SI and UE channels. First, we will introduce the LS and MMSE channel estimators. Subsequently, we present channel estimation using NN for estimating the SI and UE channels. For SI channel estimation, we correlate the received pilot signal with the pilot matrix transmitted from transmit antenna arrays, therefore, we define,

$$\widehat{\mathbf{Y}}_{\mathbf{SI}} = \mathbf{Y}_{\mathbf{SI}}\mathbf{W}^{\mathbf{H}}_{\mathbf{N_t}\times\tau}. \tag{3.18}$$

Similarly for UE channel estimation,

$$\widehat{\mathbf{Y}}_{\mathbf{UE}} = \mathbf{Y}_{\mathbf{UE}}\mathbf{W}^{\mathbf{H}}_{\mathbf{K}\times\tau}. \tag{3.19}$$

3.2.1.1 LS Channel Estimator

The LS channel estimator is the simplest channel estimation technique that does not need any prior knowledge about channel statistics and finds the channel coefficients that minimize the mean square error (MSE) between the estimated channel and the received pilot signal. The LS channel estimator can be calculated as follows:

$$\widehat{\mathbf{H}}_{\mathbf{q,LS}} = \frac{1}{\tau\sqrt{SNR_q}}\widehat{\mathbf{Y}}_{\mathbf{q}}, \tag{3.20}$$

where $q \in \{SI, UE\}$.

3.2.1.2 MMSE Channel Estimator

The MMSE is a Bayesian estimator that aims to minimize the MSE between the estimated channel and the true channel. The MMSE channel estimation technique offers improved performance compared to LS estimator. It takes into account the statistical properties of the channel and noise, resulting in better estimation accuracy, especially in the presence of noise and interference. To derive the MMSE channel estimator, we rewrite the received pilot signal for SI and UE channel estimation in a vector form:

$$vec(\mathbf{Y_{SI}}) = \sqrt{SNR_{SI}}\widetilde{\mathbf{X}}_{\mathbf{SI}}vec(\mathbf{H_{SI}}) + \sqrt{SNR_{UE}}\widetilde{\mathbf{X}}_{\mathbf{UE}}vec(\mathbf{H_{UE}}) + vec(\mathbf{N})$$

$$vec(\mathbf{Y_{UE}}) = \sqrt{SNR_{UE}}\widetilde{\mathbf{X}}_{\mathbf{UE}}vec(\mathbf{H_{UE}}) + \sqrt{SNR_{SI}}\widetilde{\mathbf{X}}_{\mathbf{SI}}vec(\mathbf{E_{SI}}) + vec(\mathbf{N}) \quad (3.21)$$

where $\widetilde{\mathbf{X}}_{\mathbf{SI}} = (\mathbf{FX_{SI}})^T \otimes \mathbf{I_{N_r}}$, $\widetilde{\mathbf{X}}_{\mathbf{UE}} = (\mathbf{X_{UE}})^T \otimes \mathbf{I_{N_r}}$. The channel covariance matrix is defined as follows:

$$\mathbf{R_q} = \mathbb{E}[vec(\mathbf{H_q})vec(\mathbf{H_q})^H]. \quad (3.22)$$

The channel covariance matrix for the MIMO channel can be related to the transmit and receive covariance matrix via the Kronecker product:

$$\mathbf{R} = \mathbf{R_t} \otimes \mathbf{R_r} \quad (3.23)$$

where $\mathbf{R_t}$ and $\mathbf{R_r}$ are the transmit and receive covariance matrices. The MMSE channel estimator of the $\mathbf{H_q}$ minimizes the MSE $\mathbb{E}\{||\mathbf{H_q} - \widehat{\mathbf{H}}_{\mathbf{q,MMSE}}||^2\}$, where the $\widehat{\mathbf{H}}_{\mathbf{q,MMSE}}$ is the MMSE estimate of $\mathbf{H_q}$, where it is given by:

$$vec(\widehat{\mathbf{H}}_{\mathbf{q,MMSE}}) = \mathbf{R_{H_qY_q}}\mathbf{R_{Y_q}}^{-1}vec(\mathbf{Y_q}) \quad (3.24)$$

where

$$\mathbf{R_{H_qY_q}} = \mathbb{E}[vec(\mathbf{H_q})vec(\mathbf{Y_q})^H], \quad (3.25)$$

$$\mathbf{R_{Y_q}} = \mathbb{E}[vec(\mathbf{Y_q})vec(\mathbf{Y_q})^H]. \quad (3.26)$$

Now, we can formulate the MMSE estimates of SI and UE channels as in the following equations:

$$\begin{aligned} vec(\widehat{\mathbf{H}}_{\mathbf{SI,MMSE}}) = \sqrt{SNR_{SI}}\mathbf{R_{SI}}\widetilde{\mathbf{X}}_{\mathbf{SI}}(SNR_{SI}\widetilde{\mathbf{X}}_{\mathbf{SI}}\mathbf{R_{SI}}\widetilde{\mathbf{X}}_{\mathbf{SI}}{}^H \\ + SNR_{UE}\widetilde{\mathbf{X}}_{\mathbf{UE}}\mathbf{R_{UE}}\widetilde{\mathbf{X}}_{\mathbf{UE}}{}^H + \mathbf{I}_{N_tN_r})^{-1}vec(\mathbf{Y_{SI}}) \end{aligned} \quad (3.27)$$

$$\begin{aligned} vec(\widehat{\mathbf{H}}_{\mathbf{UE,MMSE}} = \sqrt{SNR_{UE}}\mathbf{R_{UE}}\widetilde{\mathbf{X}}_{\mathbf{UE}}(SNR_{SI}\widetilde{\mathbf{X}}_{UE}\mathbf{R_{UE}}\widetilde{\mathbf{X}}_{\mathbf{UE}}{}^H \\ + SNR_{SI}\widetilde{\mathbf{X}}_{\mathbf{SI}}\mathbf{R_E}\widetilde{\mathbf{X}}_{\mathbf{SI}}{}^H + \mathbf{I}_{N_tN_r})^{-1}vec(\mathbf{Y_{UE}}) \end{aligned} \quad (3.28)$$

where $\mathbf{R_E}$ represents the error covariance matrix of SI cancelation, which can be calculated as:

$$\begin{aligned} \mathbf{R_E} = \mathbf{R_{SI}} - SNR_{SI}\mathbf{R_{SI}}\widetilde{\mathbf{X}}_{\mathbf{SI}}{}^H(SNR_{SI}\widetilde{\mathbf{X}}_{\mathbf{SI}}\mathbf{R_{SI}}\widetilde{\mathbf{X}}_{\mathbf{SI}}{}^H + SNR_{UE}\widetilde{\mathbf{X}}_{UE}\mathbf{R_{UE}}\widetilde{\mathbf{X}}_{UE}{}^H \\ + \mathbf{I}_{N_tN_r})^{-1}\widetilde{\mathbf{X}}_{\mathbf{SI}}\mathbf{R_{SI}} \end{aligned} \quad (3.29)$$

3.2.1.3 NN Channel Estimator

Although conventional channel estimation techniques such as MMSE can leverage the spatial correlation present in large antenna arrays, they require prior knowledge of the channel covariance matrix and are computationally intensive due to matrix inversion involving a large matrix. In various fields of research, it has been demonstrated that DNNs can possibly utilize the inherent structure of data by solely observing a sufficient number of data points. Different network architectures, such as fully convolutional neural networks (FCNNs), convolutional neural networks (CNNs), recurrent neural networks (RNNs), etc., can be utilized depending on the characteristics of the data. For instance, CNNs are suitable for addressing problems with feature correlation and local dependencies among them, while RNNs are more effective for handling memory-based features like time series.

It has been shown in various studies that the wireless channel with large antenna arrays is spatially correlated, see e.g., [SE+20]. To exploit this spatial correlation for channel estimation, we employ CNNs which are well known for capturing the local dependency of features among data points.

The input to the CNN is the correlated received pilot signal, i.e., $\widehat{\mathbf{H}}_{\mathbf{q}}$, and the output is the estimated channel, $\widehat{\mathbf{H}}_{\mathbf{q,NN}}$, $q \in \{SI, UE\}$. In convolutional layers, we apply a 3×3 window size sliding through the whole input features with a unit stride size. Different numbers of convolutional hidden layers are employed, and each layer applies a different number of filters to extract features from the successive windows of its input features. The number of filters and hidden layers in the convolutional layers will be carefully designed in Section 4.2.

To keep the dimension of the output and the input unchanged, we utilize padding after convolution processing. We apply rectified linear units (ReLU) functions as the activation function for the hidden layers, while for the output layer, the linear activation function is used. Since tensors do not support complex operations, the input to the CNN is converted to three-dimensional tensors, where the third dimension stores the real and imaginary parts of the complex data samples. Therefore, if we define $\mathbf{X}_{\mathbf{tr}}$ and $\mathbf{Y}_{\mathbf{tr}}$ as the input and labels of the CNN during training, we have:

$$\mathbf{X}_{\mathbf{tr}}[:,:,0] = \Re\{\widehat{\mathbf{Y}}_{\mathbf{q}}\},$$

$$\mathbf{X}_{\mathbf{tr}}[:,:,1] = \Im\{\widehat{\mathbf{Y}}_{\mathbf{q}}\},$$

$$\mathbf{Y}_{\mathbf{tr}}[:,:,0] = \Re\{\mathbf{H}_{\mathbf{q}}\},$$

$$\mathbf{Y_{tr}}[:,:,1] = \Im\{\mathbf{H_q}\}. \tag{3.30}$$

For training of CNN, a dataset consisting of M_{tr} samples is generated with $(\widehat{\boldsymbol{Y}}_{\mathbf{q}}{}^{(n)}, \mathbf{H_q}{}^{(n)})$ representing the n-th sample. We employ supervised learning, where $\mathbf{H_q}$ is regarded as the label during training. We apply min-max scaling to scale the dataset in the range $(0,1)$. Such normalization is highly recommended for training machine learning models. We consider the MSE loss function, and the objective of training is minimizing this loss function:

$$\mathrm{MSE} = \frac{1}{M_{tr}} \sum_{i=1}^{M_{tr}} ||\mathbf{X_{tr}} - \mathbf{Y_{tr}}||_F^2. \tag{3.31}$$

3.2.2 RX-TX Channel Mapping

Since in separate antenna configuration, two different antenna arrays are utilized for uplink reception and downlink transmission, uplink and downlink channel experiences different channel realization. So far, we have assumed that RX arrays at BS receive pilot signals from both uplink and downlink UEs and estimate all channels from both uplink and downlink UEs to the RX arrays. For downlink transmission, transmit antenna arrays need the channel state information (CSI) of the transmit antenna arrays to downlink UEs. The transmit antenna arrays are not capable of receiving and processing pilot signals and implementing a separate receive RF chain and ADC at the transmit antenna arrays for just pilot processing due to the cost. As a result, we need to somehow map the channel between the RX arrays and downlink UEs to the TX array and the downlink UEs. Due to the multi-path effect and random scattering environment, it is not straightforward to derive mathematically the relation of such mapping. More specifically, if we assume that the RX-UE channel is:

$$\mathbf{h}_{\mathbf{UE,RX}} = \sqrt{\frac{1}{N_r}} \sqrt{\beta} \sum_{i=0}^{P-1} \alpha_i \mathbf{a}_{\mathbf{a}}(\theta_{\mathbf{i}}), \tag{3.32}$$

$\mathrm{a}_{\mathrm{a}}(\theta)$ is the uniform linear array (ULA) responses of receive antennas, given by

$$\mathbf{a}_a(\theta) = \sqrt{\frac{1}{N_r}} \left[1, \ldots, \exp\left(j2\pi \frac{d}{\lambda}(N_r - 1)\sin\theta\right)\right]^T, \tag{3.33}$$

θ is the angle of arrival (AoA) to the receive antenna arrays at BS, d and λ are the antenna spacing and wavelength, respectively. We assume AoA follow the local scattering model with a uniform distribution $\left[-\frac{\theta_{AS}}{2}, \frac{\theta_{AS}}{2}\right]$, where θ_{AS} is the angular spread (AS) of the multi-path components.

As shown in the following Figure 7, transmit and receive arrays are at a close distance in the order of a few wavelengths from each other. Therefore, the channel amplitude is the same for both receive and transmit antenna arrays, while the antenna separation will create a delay depending on the AoA of each path. Thus, the TX-UE channel will be:

$$\mathbf{h}_{\mathbf{UE,TX}} = \sqrt{\frac{1}{N_t}}\sqrt{\beta}\sum_{i=0}^{P-1} \alpha_i \mathbf{a}_{\mathbf{d}}(\theta_{\mathrm{i}}) e^{j\frac{2\pi}{\lambda} l cos\theta_i}, \tag{3.34}$$

$\mathrm{a_d}(\theta)$ is ULA responses of transmit antennas, given by

$$\mathbf{a}_d(\theta) = \sqrt{\frac{1}{N_t}}\left[1, \dots, \exp\left(j2\pi\frac{d}{\lambda}(N_t - 1)\sin\theta\right)\right]^T, \tag{3.35}$$

θ is the angle of departure (AoD) from the transmit antenna arrays at BS. Similarly, we assume AoD follow the local scattering model with a uniform distribution $\left[-\frac{\theta_{AS}}{2}, \frac{\theta_{AS}}{2}\right]$.

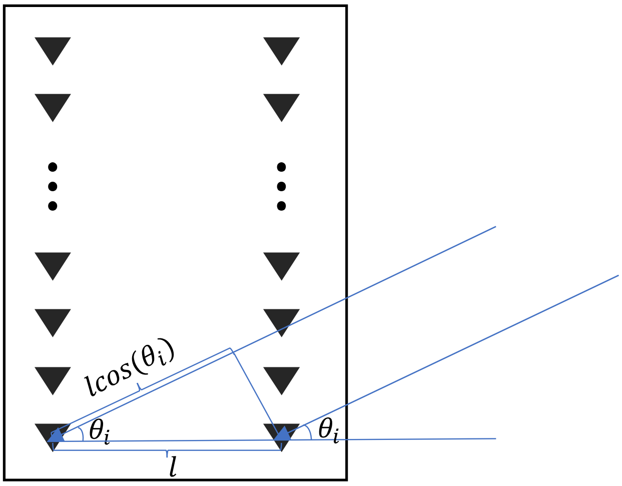

Figure 7: Phase shift between receive and transmit antenna arrays in separate antenna configuration in full-duplex BS.

The mathematical relationship between $\mathbf{h}_{\mathbf{UE,TX}}$ and $\mathbf{h}_{\mathbf{UE,RX}}$ is not well-defined due to the random AoA and the effects of multi-path propagation. Based on universal theory approximation [KM+89], any feedforward neural network is capable of approximating any continuous function. This theory suggests that, given enough computational resources and data, it is possible to build machine learning models that can accurately approximate any function that maps input to output. Therefore, universal theory approximation inspires us to seek if it is possible to map the channel of RX antenna arrays and downlink UEs to the channel of TX antenna arrays and downlink UEs. Furthermore, recent studies [AA19] have demonstrated the existence of a space mapping function that can effectively map the channel from one set of antenna arrays to another. As a result, we employ a NN to approximate this mapping function based on the principles of universal theory approximation.

To accomplish this, we utilize an FCNN similar to the network used for estimating UE channels. Similar to CNN, we explore different numbers of hidden layers with the ReLU activation function in Section 4.2. The input for FCNN is the channel between receive antenna array and UEs and the output is the channel between transmit antenna array and UEs. Therefore, for the training of FCNN, we gather M_{tr} samples of $\mathbf{h}_{\mathbf{UE,RX}}$ as the input and $\mathbf{h}_{\mathbf{UE,TX}}$ as the corresponding label. Again, we apply min-max normalization and MSE loss function to optimize the mapping from the channel of RX arrays and Ues to the channel of TX arrays and Ues. We create the following data samples as the input and label of FCNN to work with real-value tensors,

$$\mathbf{x}_{\mathbf{tr}}[0\colon N_r] = \Re\{\mathbf{h}_{\mathbf{UE,RX}}\},$$

$$\mathbf{x}_{\mathbf{tr}}[N_r\colon 2N_r] = \Im\{\mathbf{h}_{\mathbf{UE,RX}}\},$$

$$\mathbf{y}_{\mathbf{tr}}[0\colon N_r] = \Re\{\mathbf{h}_{\mathbf{UE,TX}}\},$$

$$\mathbf{y}_{\mathbf{tr}}[N_r\colon 2N_r] = \Im\{\mathbf{h}_{\mathbf{UE,TX}}\}. \tag{3.36}$$

3.3 RIS-NOMA Network

In this section, we first describe the system and signal model for our considered RIS-NOMA system.

3.3.1 System Model

We consider an uplink transmission RIS-NOMA system where the BS is equipped with a single antenna, an RIS with N elements, a jammer with M antennas, and two single antenna users using PD-NOMA, as shown Figure 8. The received signal at the BS can be written as:

$$r = \sum_{\mathrm{i}=1}^{2} (\mathrm{h_i} + \mathbf{f}^{\mathrm{T}}\boldsymbol{\Phi}\mathbf{g}_{\mathrm{i}})\mathrm{x_i} \quad + \left(\mathbf{h}_{\mathrm{j}}^{\mathrm{T}} + \mathbf{f}^{\mathrm{T}}\boldsymbol{\Phi}\mathbf{G}_{\mathrm{j}}\right)\mathbf{x}_{\mathrm{j}} + \mathrm{n_r}\,, \tag{3.37}$$

where $h_i \in \mathbb{C}^{1\times 1}$ denotes the direct channels between the users and the BS, x_i is the symbol transmitted by user i, $\mathbf{f} \in \mathbb{C}^{1\times 1}$ denotes the channel vector between the RIS and the BS, $\boldsymbol{\Phi} = diag\{e^{j\theta_1}, e^{j\theta_2}, \dots, e^{j\theta_N} \in \mathbb{C}^{N\times N}\}$ is the diagonal matrix containing the RIS phase-shifts, $\theta_n \in [0, 2\pi]$ is the phase shift of the n-th reflecting elements, $\boldsymbol{g}_i \in \mathbb{C}^{N\times 1}$ denotes the channel vector between user i and the RIS, $\mathbf{h}_\mathrm{j} \in \mathbb{C}^{M\times 1}$ denotes the channel vector between the jammer and the BS, $\mathbf{G}_\mathrm{j} \in \mathbb{C}^{N\times M}$ denotes the channel matrix between the jammer and RIS, $\mathbf{x}_\mathrm{j} \in \mathbb{C}^{M\times 1}$ is the signal transmitted by the jammer, and $n_r \sim CN(0,\sigma^2)$ is the AWGN. We define the transmit power of each user as $p_i = E(|x_i|^2)$.

Assuming that UE_1 has the strongest channel and using a sufficiently large transmit power level p_1 fulfilling the condition in Figure 3, $p_1|h_1|^2 > p_2|h_2|^2$, the BS would first decode the signal for UE_1 treating the interference by the signal from UE_2 as AWGN, and then subtracting it from the received signal r when decoding the signal from UE_2 . Thus, the signal to interference plus noise ratio (SINR) of UE_1 is given by,

$$\gamma_1 = \frac{p_1 \mid h_1 + \mathbf{f}^T \mathbf{\Phi} \mathbf{g}_1 \mid^2}{p_2 \mid h_2 + \mathbf{f}^T \mathbf{\Phi} \mathbf{g}_2 \mid^2 + \sigma_\mathrm{j}^2 + \sigma^2}. \tag{3.38}$$

where σ_j^2 denotes the power of the jammer signal received by the BS. This term will be derived in subsection 0 under the assumption of perfect SIC of the UE_1 signal, i.e., no error propagation, the SINR for UE_2 can be written as

$$\gamma_2 = \frac{p_2|h_2+\mathbf{f}^T\mathbf{\Phi}\mathbf{g}_2|^2}{\sigma_\mathrm{j}^2+\sigma^2}. \tag{3.39}$$

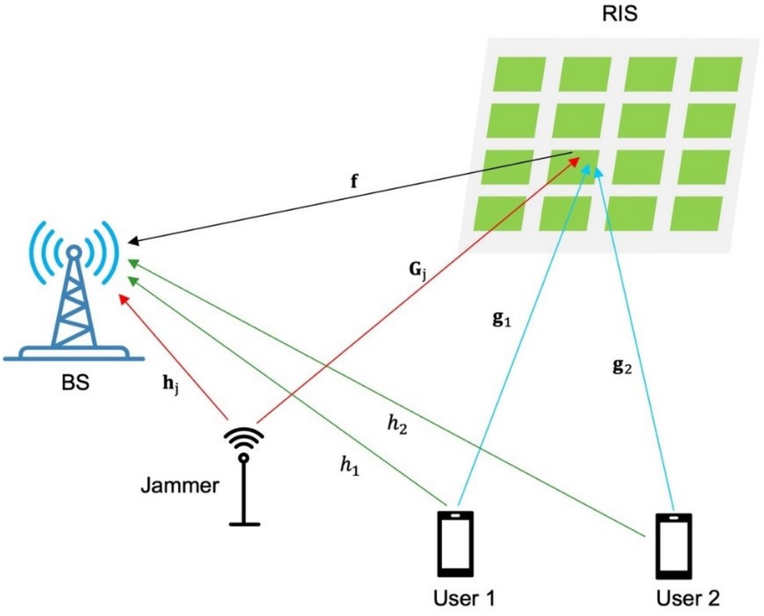

Figure 8: Illustration of RIS-NOMA aided two users uplink communication.

3.3.2 Absorptive RIS

As mentioned above, recent work has considered RIS implementations in which not all energy is reflected. In prior work, the non-reflected energy is either transmitted or ‘’refracted" to the other side of the RIS, or it is demodulated and sampled for channel estimation or sensing purposes. Here, we simply assume that the RIS absorbs an adjustable fraction of the incoming energy at each element, without assuming that the absorbed energy is used for any other purpose. We will see that the ability to adjust the magnitude of the reflected power at each RIS element provides additional degrees of freedom (DoFs) that are particularly useful in situations where interference mitigation is required. Mathematically, the A-RIS model assumes that the reflection coefficient of each RIS element can be described as $\beta_n e^{j\theta_n}$, where $0 \leq \beta_n \leq 1$ describes the amplitude of the reflected signal component. Such a constraint has numerical advantages as it is convex. In practice, the value of β_i, like θ_n, may have to be quantized, and the two variables are very likely to be coupled, meaning that changes to one will affect the other. For this initial study, we ignore such effects to investigate the potential gains in an idealized scenario.

3.3.3 Smart Jammer Modeling

We assume a ‘’smart’’ jammer that is aware of Φ and the CSI of all the channels used by the jammer, i.e., $\mathbf{h}_\mathrm{j}$, $\mathbf{f}$, $\mathbf{G}_\mathrm{j}$, and whose goal is to choose $\boldsymbol{x}_\mathrm{j}$ such that the interference power at the BS is maximized. In other words, the jammer designs $\boldsymbol{x}_\mathrm{j}$ based on the following problem:

$$\max_{\mathbf{x}_\mathrm{j}} \quad \|(\mathbf{h}_\mathrm{j}^\mathrm{T} + \mathbf{f}^\mathrm{T}\mathbf{\Phi}\mathbf{G}_\mathrm{j})\mathrm{x}_\mathrm{j}\|. \quad \text{s.t.} \quad \mathrm{E}(\|\mathrm{x}_\mathrm{j}\|^2) \leq \mathrm{P}_\mathrm{j} \tag{3.40}$$

where P_j is the per antenna jammer transmit power. The solution to this problem is $\mathbf{x}_\mathrm{j} = (\sqrt{\mathrm{P}_\mathrm{j}}/\rho)(\mathbf{h}_\mathrm{j}^\mathrm{T} + \mathbf{f}^\mathrm{T}\mathbf{\Phi}\mathbf{G}_\mathrm{j})^\mathrm{H}$, where $\rho = \|\mathbf{h}_\mathrm{j}^\mathrm{T} + \mathbf{f}^\mathrm{T}\mathbf{\Phi}\mathbf{G}_\mathrm{j}\|$. Thus, the term due to jamming in the denominator of the SINR expressions (3.35) and (3.36) becomes:

$$\sigma_j^2 = \mathrm{P}_\mathrm{j}\|\mathbf{h}_\mathrm{j}^\mathrm{T} + \mathbf{f}^\mathrm{T}\mathbf{\Phi}\mathbf{G}_\mathrm{j}\|^2. \tag{3.41}$$

3.3.4 Optimization Problem

There are several ways to illustrate the benefit of the A-RIS in the problem under consideration. Here, we study the problem of minimizing the total transmit power of the users such that given SINR quality-of-service constraints of the users are met. The problem can be formulated mathematically as follows:

$$min\ (p_1 + p_2) \text{ such that}$$

$$\mathbf{C1}: p_1 \geq 0$$

$$\mathbf{C2}: p_2 \geq 0$$

$$\mathbf{C3}: \frac{p_1 \mid h_1 + \mathbf{f}^T \mathbf{\Phi} \mathbf{g}_1 \mid^2}{P_{\mathrm{j}} \| \mathbf{h}_j^T + \mathbf{f}^T \mathbf{\Phi} \mathbf{G}_{\mathrm{j}} \|^2 + p_2 \mid h_2 + \mathbf{f}^T \mathbf{\Phi} \mathbf{g}_2 \mid^2 + \sigma^2} \geq T_1 \qquad (3.42)$$

$$\mathbf{C4}: \frac{p_2 \mid h_2 + \mathbf{f}^T \mathbf{\Phi} \mathbf{g}_2 \mid^2}{P_{\mathrm{j}} \| \mathbf{h}_j^T + \mathbf{f}^T \mathbf{\Phi} \mathbf{G}_{\mathrm{j}} \|^2 + \sigma^2} \geq T_2$$

$$\mathbf{C5}: 0 \leq \beta_n \leq 1, n = 1, \cdots, N$$

$$\mathbf{C6}: 0 \leq \theta_n \leq 2\pi, n = 1, \cdots, N$$

where the constraints $\mathbf{C1}$ and $\mathbf{C2}$ ensure that the transmitted power is non-negative, $\mathbf{C3}$ and $\mathbf{C4}$ correspond to the desired SINR constraints for user 1 (T_1) and user 2 (T_2) respectively, and $\mathbf{C5}$ and $\mathbf{C6}$ enforce the properties of the A-RIS. When we consider the performance of a conventional phase only RIS, constraint $\mathbf{C5}$ is replaced with $\beta_n = 1$. As seen in (3.39), the resulting objective function and constraints are both non-linear and non-convex, so we address this problem using numerical optimization.

3.4 Resources Allocation in IAB Networks

In this section, we describe the system model and algorithmic framework of Stackelberg game.

3.4.1 System Model

We consider an IAB heterogeneous network (HetNet). As shown in Figure 9, this network consists of N nodes, where the node index in the network is $n \in \boldsymbol{\mathcal{A}}$, where $\boldsymbol{\mathcal{A}} = \{1, 2, 3, \dots, N\}$. Set $\boldsymbol{\mathcal{A}}$ contains 2 subsets of nodes: (i) the subset of donor nodes consists of D nodes, which represent macro base stations (MBSs) in the mobile network, and (ii) the IAB nodes subset consists of K nodes, which represent the small BSs (SBSs) that surround the MBSs. In this network, only the MBSs are connected through optical fiber to the core network and the SBSs use wireless connections for the backhaul link to connect each other and to connect with the MBSs. The connection between the nodes could be one hop or multi-hop. Every node $n \in \boldsymbol{\mathcal{A}}$ is considered to has a known load described in load set

$\boldsymbol{\mathcal{L}} = \{L_1, L_2, \dots, L_N\}$. The IAB architecture is based on a hierarchical or a cyclical structure, where it is well-defined if a certain node is “above/parent” or “below/child”.

We consider the information flows in the downlink directions. We assume that each node has multiple connections with the other surrounding nodes, but one connection will be adopted for simplicity, and a donor node does not have any connection to other donor nodes in the network. The link between each pair of nodes i and j has a defined capacity W_{ij}.

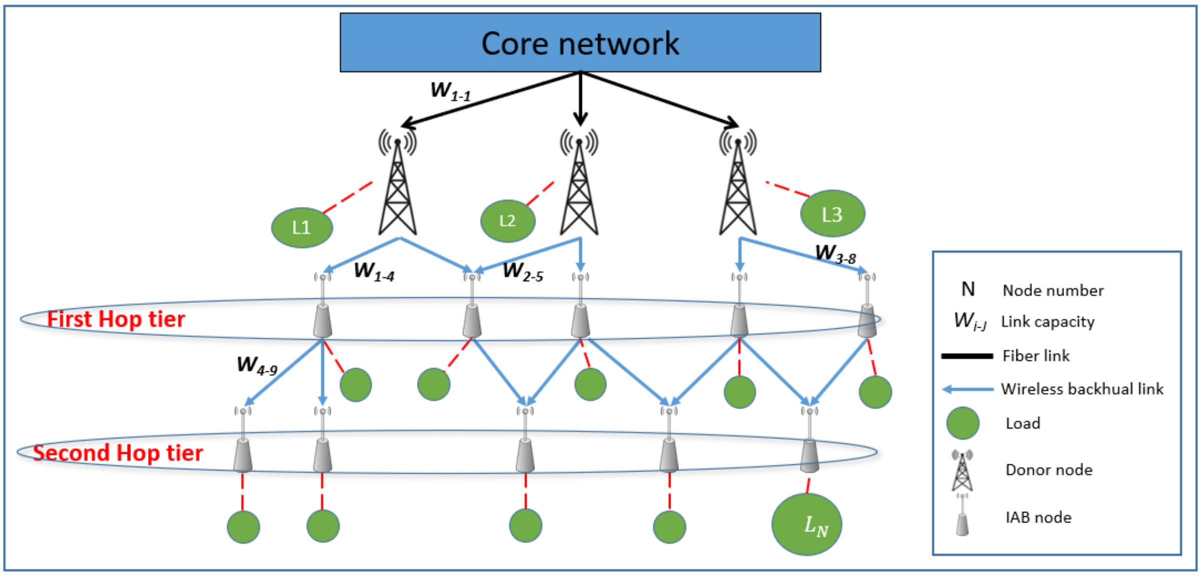

Figure 9: Schematic system model of IAB HetNet.

3.4.1.1 Node Load

The load of each node includes the load generated by the end-users connected to this node in addition to the load of other nodes passed from this node. The load can be considered as an instantaneous value at each time slot or average value during a time duration. Channel conditions such as interference and noise are not considered in our study.

The network-wise load set $\boldsymbol{\mathcal{L}}$ plays a key role in the performance modelling, where a well-designed network shall be able to meet the target scenarios with the optimum offloading strategies.

3.4.1.2 Link Capacity

Link capacity W_{ij} is the maximum amount of traffic that a link can handle between node i and node j. The capacity is assumed to be an abstract value that is independent from the network constraints like: the distance between the nodes, or the SINR.

3.4.1.3 The Connectivity Matrix (CM)

By defining the connections between the nodes in the IAB network, the matrix dimension is $N \times N$ and its elements $\boldsymbol{CM}$ values are assigned based on the link capacities W_{ij}. The values of $\boldsymbol{CM}$ members are determined based on the following rules:

- Equal to zero if there is no connection between node i and node j.
- Equal to the link capacity weight if there is a connection between the nodes.
- The main diameter elements will equal to zero for the normal IAB nodes, while they will equal to the link capacity for the IAB donor nodes that is connected to the core network.

We denote by $\mathcal{E}_i^-$ and $\mathcal{E}_i^+$ the set of outgoing and incoming arcs of node i, respectively. The previous considerations lead to CM for the one hop connection with the following formula:

$$CM_{ij} = \begin{cases} W_{ij}\,; if \;\; i \; and \; j \; are \; connected \\ \qquad 0\,; otherwise \end{cases} \tag{3.43}$$

$$\boldsymbol{CM} = \begin{bmatrix} \boldsymbol{W_{1,1}} & \boldsymbol{0} & \dots & \boldsymbol{0} & \boldsymbol{W_{1,D+1}} & \dots & \boldsymbol{W_{1,N}} \\ \boldsymbol{0} & \boldsymbol{0} & \dots & \boldsymbol{0} & \boldsymbol{W_{2,D+1}} & \dots & . \\ \boldsymbol{0} & \boldsymbol{0} & \dots & \boldsymbol{0} & \dots & \dots & . \\ \boldsymbol{0} & \boldsymbol{0} & \dots & \boldsymbol{W_{D,D}} & \dots & \dots & . \\ \boldsymbol{0} & \boldsymbol{0} & \dots & \boldsymbol{0} & \boldsymbol{W_{D+1,D+1}} & \dots & \boldsymbol{W_{D+1,N}} \\ . & . & . & . & . & \dots & . \\ . & . & . & . & . & \dots & . \\ . & . & . & . & . & \dots & . \\ \boldsymbol{0} & \boldsymbol{0} & \dots & \boldsymbol{0} & \boldsymbol{0} & \dots & \boldsymbol{W_{N,N}} \end{bmatrix} \tag{3.44}$$

where N is the total number of nodes in the topology, and D is the number of donor nodes. The donor nodes are the first D elements in the connectivity matrix. The elements below the main diagonal of $\boldsymbol{CM}$ are zero because $\boldsymbol{CM}$ represents the down link case only.

To distinguish donor nodes from normal ones, we assume that the main diagonal of $\boldsymbol{CM}$ equal to the node capacity of donor nodes and equal to zero for normal nodes, i.e.,

$$CM_{ii} = \begin{cases} W_{ii}; if\ i\ \leq D \\ 0\ ; otherwise \end{cases}. \tag{3.45}$$

There is no connection between donor nodes, i.e.,

$$CM_{ij} = 0; if\ i\ \leq D\ and\ j \leq D\ and\ i \neq j. \tag{3.46}$$

The connectivity matrix represents an input to the proposed method. The proposed method will then manipulate the connectivity matrix in addition to other parameters such as load and requirements and give the solution. The solution includes among many outputs a new version of the connectivity matrix that determines the best paths for each node. In this matrix, each node will connect only with one donor node.

The output connectivity matrix includes a set $\boldsymbol{\mathcal{S}} = \{\mathcal{S}_1, \mathcal{S}_2, \dots\}$ of disjointed spanning trees. Each spanning tree contains at least one donor node. A matrix element with a zero value in the original connectivity matrix will remain zero in the output connectivity matrix. Other matrix elements will take the same values as in the original matrix if they belong to the same spanning tree, and zeros otherwise. In other words, if node i is from spanning tree $\mathcal{S}_p$ $(i \in \mathcal{S}_p)$, and node j is from spanning tree $\mathcal{S}_q(j \in \mathcal{S}_q)$, the element CM'_{ij} is determined as:

$$CM'_{ij} = \begin{cases} CM_{ij}\ ; if\ \ p = q \\ \ 0\ ; otherwise \end{cases} \tag{3.47}$$

Given the problem statement, we can construct a Stackelberg game to optimize the network topology of the IAB HetNet. The leaders in this game would be the MBSs (D nodes) or SBSs (K nodes), and the followers would be the SBSs (K nodes). The leaders will make decisions to optimize their own utility, considering the potential reactions of the followers.

3.4.2 Stackelberg Game Design

Stackelberg game is a strategic game that models a scenario with both leaders and followers interacting sequentially. It is a bi-level optimization problem where the leaders make their decisions first, followed by the reactions of the followers. In this game, there are two types of players: leaders and followers. The leaders move first by choosing their optimal strategies, considering how the followers may react. After observing the leaders' moves, the followers then choose their best responses to optimize their own utilities, given the leaders' pre-committed strategies.

This hierarchical decision-making process is captured via the concept of 'Stackelberg equilibrium'. It is the sub-game perfect Nash equilibrium of the extended game where the followers anticipate the leaders' moves. For the equilibrium to exist, the leaders strategize to maximize their utility by looking ahead at the potential follower reactions, while followers optimize by considering the leader strategies as constraints. The equilibrium achieves stability as no player can benefit by deviating unilaterally from the prescribed strategies considering how others play.

By modeling leadership influence, it generalizes Nash equilibrium to strategic scenarios with asymmetric information and bargaining power. Stackelberg games have wide applications in economics, security, supply chain management and other hierarchical decision problems.

3.4.2.1 Players

There are two types of players: providers (leaders), and consumers (followers). When the interaction is between Macro Base Stations (MBSs/D nodes) and Small Base Stations (SBSs/K nodes), we consider the first as leaders, and the later as followers. When the interaction is between some MBSs, the MBSs which serve the other MBSs become leaders, and the MBSs which get the service are considered as followers.

3.4.2.2 Strategies

The following strategies have been taken into account:

- The Leaders select a subset of consumers (SBSs) to connect to, considering their capacity (W_{ij}) and current load (L_i). The leaders want to optimize their connections to minimize the load and maximize the capacity.
- The Followers select a provider (MBS or SBS) to connect to based on the decision of the leader. The followers want to connect to a leader that optimizes their own utility, considering their current load and the capacity of the connection.
- The considered structure is multi-level connections, where MBSs are at the high level and the first level of SBSs is connected to the MBS as followers, and they connected to the second level of SBSs as leaders, where they provide the second level of SBSs with a capacity.

3.4.2.3 Payoff Functions

The leaders' utility function can be defined as:

$$U_D = W_{ij} - \alpha L_i \tag{3.48}$$

where W_{ij} represents the capacity of the connection between leader node i and SBS j, L_i represents the current load on leader node i, and α is a weighting factor that determines the trade-off between maximizing capacity and minimizing load.

The utility function of the leaders captures their objective of maximizing the capacity of their connections while minimizing their own load. The term W_{ij} represents the positive utility gained from having a high-capacity connection, while the term αL_i represents the negative utility incurred from a high load on the leaders. Followers' utility function: it can be defined as:

$$U_K = W_{ij} - \beta L_j \tag{3.49}$$

where W_{ij} represents the capacity of the connection between leader node i and SBS j, L_j represents the current load on the follower SBS j, and β is a weighting factor that determines the trade-off between maximizing capacity and minimizing load.

The utility function for the followers reflects their objective of maximizing their own utility based on the capacity of the connection and their own load. The term W_{ij} represents the positive utility gained from having a high-capacity connection to their chosen providers, while the term βL_j represents the negative utility incurred from a high load on the SBS.

These utility functions can be customized further based on the specific requirements and characteristics of the IAB HetNet scenario under consideration. The choice of weighting factors (α and β) will depend on the relative importance assigned to capacity and load in the decision-making process.

3.4.2.4 Nash Equilibrium Existence

Given the described Stackelberg game, we can prove the existence of a Nash Equilibrium by showing that the game is a potential game. A potential game is a game which has a potential function, which is from the set of strategies to the real numbers, such that any player's marginal incentives to change their strategy (keeping others' strategies fixed) coincide with the change in the potential function. In potential games, a Nash Equilibrium always exists. Formally, given a game with a finite set of n players, each having a finite set of actions, and a real-valued payoff function for each player, the game is a potential game if there exists a function $\boldsymbol{\Phi}: \boldsymbol{A1} \times \boldsymbol{A2} \times \ldots \times \boldsymbol{An} \rightarrow \boldsymbol{R}$, where A$i$ is the set of actions for player i, such that for any players i and j, any action profile a and b that differ only in the action of player i, the difference in the payoff for player i caused by changing his action from a to b is the same as the difference in the potential function:

$$U_i(b) - U_i(a) = \Phi(b) - \Phi(a) \tag{3.50}$$

where U_i represents the utility function for player i.

Now, let's consider the utility functions for the leaders and followers in the given Stackelberg game:

$$U_D = W_{ij} - \alpha L_i \text{ for the leaders}$$

$$U_K = W_{ij} - \beta L_j \text{ for the followers} \tag{3.51}$$

We can construct a potential function Φ based on these utility functions as follows:

$$\Phi = \sum_j (W_{ij} - \alpha L_i) + \sum_k (W_{kj} - \beta L_j) \tag{3.52}$$

where the first summation is over all j (followers/SBSs) and the second summation is over all k (leaders/MBSs).

Now, if a leader i changes its strategy, its payoff change U_D would be:

$$\Delta U_D = \Delta W_{ij} - \alpha \Delta L_i \tag{3.53}$$

The change in the potential function would be:

$$\Delta\Phi = \Delta \sum_j (W_{ij} - \alpha L_i) + \Delta \sum_k (W_{kj} - \beta L_j) \tag{3.54}$$

As we can see, $\Delta U_D = \Delta\Phi$ for the leader i. Similarly, we can show that when a follower j changes its strategy, its payoff change U_K equals the change in the potential function $\Delta\Phi$. Hence, the given Stackelberg game is a potential game and, therefore, a Nash Equilibrium exists.

4 Performance evaluation and experimentation

4.1 Evaluation of Machine Learning based mmWave Beam Prediction

In this section, we evaluate the performance of our proposed algorithm and compare it with the state of the art. More specifically, we define dataset generation, simulation parameters, considered scenarios, key performance indicators (KPIs) for performance evaluation, followed by the performance evaluation and comparison.

4.1.1 Simulation Parameters and Dataset Generation

For dataset generation, we utilize exhaustive beam search (EBS) and multi-resolution hierarchical beam search (HBS). The training dataset consists of RSRP values obtained via HBS and the labels are obtained via EBS. During training, the task for the ML model is to learn the relation between RSRP values and the ideal beam IDs. During the inference only, the RSRP values are provided to the input of ML model, and the ML model infers the optimal beam IDs. Simulation parameters are detailed in Table 2.

Table 2: List of simulation parameters of machine learning based mmWave beam prediction.

Parameter	**Values**
No. of BS antennas M_{TX}	64
No. of UE antennas M_{RX}	8
BS codebook size N_{TX}	64
UE codebook size N_{RX}	8
Transmit power P	30 dBm
Center frequency f_c	28 GHz
Bandwidth B	100 MHz
Noise power σ^2	$174 + \ 10log_{10}\ B\ + N_F$
Pathloss model	$20\log_{10} d + 20\log_{10} f_c - 147.56$
Channel model	Clustered Delay Line (CDL)

To evaluate generalization capabilities of proposed model, we consider following three scenarios:

- **Scenario 1**: The ML model is trained with a dataset created by utilizing CDL-D channel profile and ML model testing is done on CDL-D channel profile.
- **Scenario 2**: The ML model is trained with a dataset created by utilizing CDL-D channel profile and ML model testing is done on CDL-E channel profile.

- **Scenario 3**: The ML model is trained with a dataset created by utilizing CDL-D and CDL-E channel profile and ML model testing is done on CDL-D and CDL-E channel profile.

The dataset consists of 25000 data samples, where 70% is used for training, 10% for validation, and 20% for testing. Further, we consider mean squared error as the loss function and the model is trained via Adam optimizer.

4.1.2 Key Performance Indicators

We evaluate and compare the performance of our proposed model in terms of beam prediction accuracy, beam measurement overhead, and average achieved RSRP. The beam prediction accuracy is defined as the percentage that the optimal beam is among the K best beam predicted by the ML model. The beam measurement overhead is defined as the ratio of $\frac{N}{M}$, where N is the number of measurements required by the ML model and M is the number of total beams to be predicted. Further, for complexity comparison of our proposed model, we use number of trainable parameters and model size as the KPI.

4.1.3 Simulation Results

For performance evaluation, in addition to the traditional EBS and HBS, we compare the performance of our proposed model with a CNN based approach from [ECB+21] and fully connected ANN based approach in [HA21].

4.1.3.1 Performance Evaluation

Figure 10 evaluates the performance in terms of beam prediction accuracy and beam measurement overhead. In terms of beam prediction accuracy, EBS achieves highest beam prediction accuracy. However, this accuracy is achieved at the cost of higher beam measurement overhead. Further, HBS achieves an accuracy of around 94% but at the cost of additional delay as HBS requires two measurement cycles to identify the best beam. For ML Top-1, the proposed model achieves similar accuracy as other ML models but with significantly lower computational complexity as discussed in the next sections. Additionally, ML methods achieve less accuracy as compared to EBS but ML methods incur significantly lower beam measurement overhead as shown on the right hand axis of Figure 10. Figure 11 shows the average achieved RSRP of our proposed model. Here, it can be observed that all the approaches achieve similar RSRP indication that ML methods with much lower beam measurement overhead can achieve similar performance as EBS with full measurement overhead.

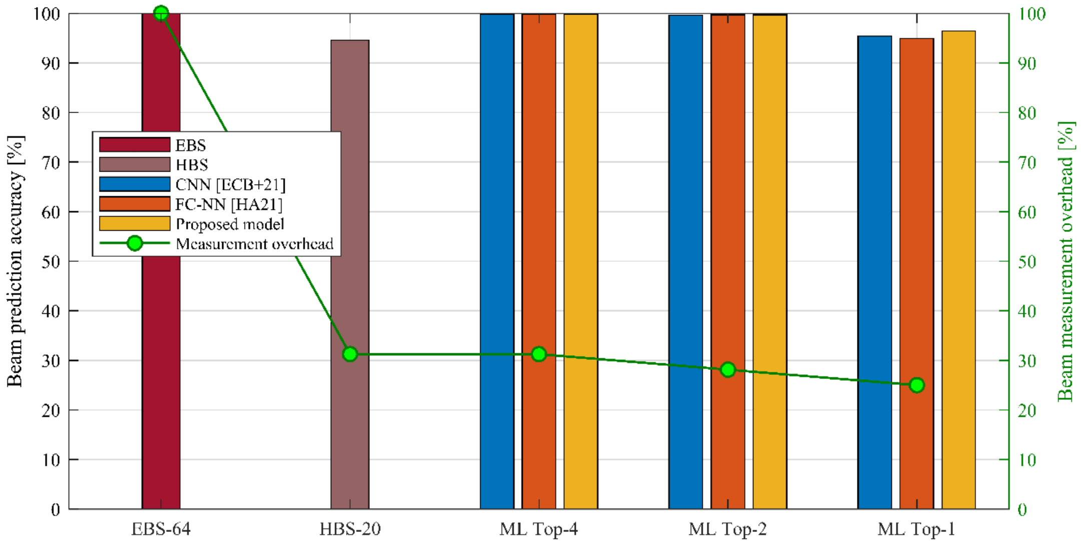

Figure 10: Comparison of beam prediction accuracy and beam measurement overhead.

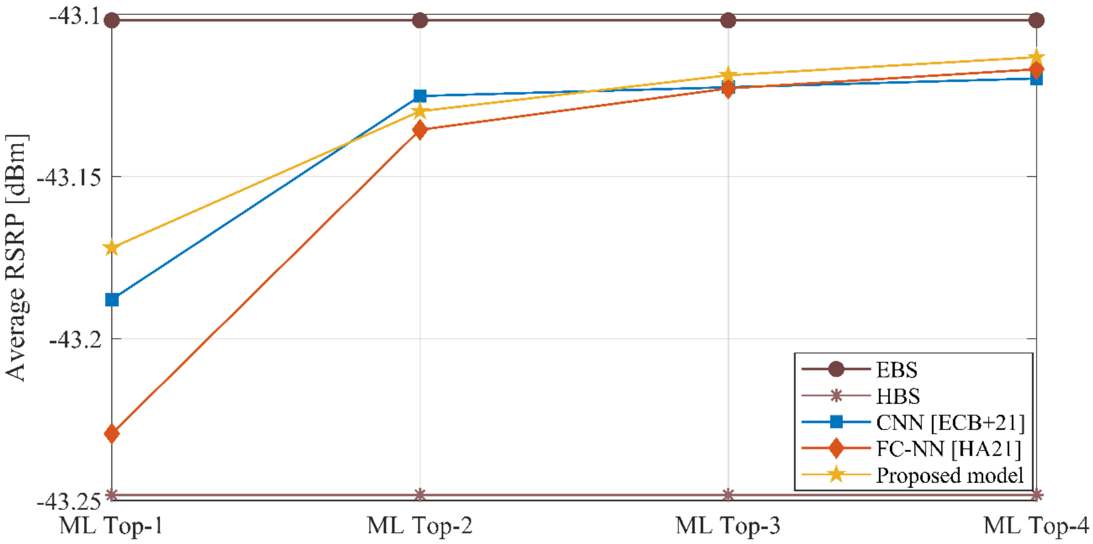

Figure 11: Comparison of average achieved RSRP [dBm].

We now evaluate generalization capabilities of our proposed model based on the scenarios defined earlier. Figure 12 shows that the performance of the ML model reduces by around 7% over scenario 2. It is because of the different channel profiles during training and testing. Furthermore, it can be observed that the performance of the ML model improves over scenario 3 when the ML model is trained and tested on combined dataset from different channel profiles. However, the performance in scenario 3 is still less as compared to scenario 1. This indicates that there exists a tradeoff between ML model prediction accuracy and its generalization capabilities.

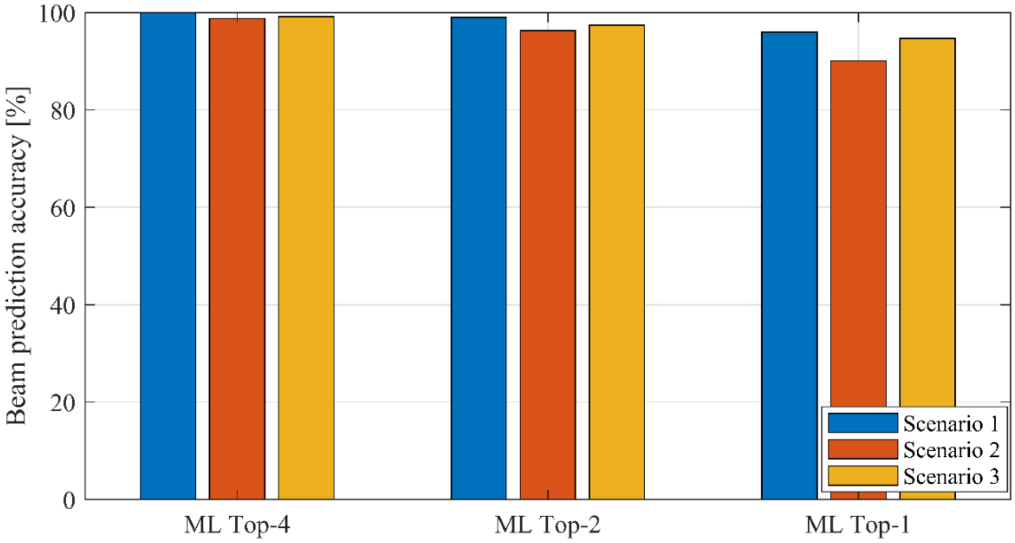

Figure 12: Analysis of generalization capabilities of proposed model.

4.1.3.2 Complexity Analysis

For evaluating and comparing the performance of our proposed model, we now compare its complexity with other approaches. For complexity of an ML model, the number of trainable parameters is an important measure. Additionally, we also compare complexity in terms of model size by assuming 32-bit precision.

Table 3 presents the complexity comparison of our proposed model with the state of the art. Here, it can be observed that the proposed model benefits from much lower computational complexity as compared to other ML-based approaches. The reduced complexity of our proposed model allows faster beam prediction and reduced retraining time.

Table 3: Complexity comparison between different machine learning based mmWave beam prediction algorithms.

	Number of Trainable Parameters	**Model Size (Mbits)**
CNN from [ECB+21]	352,034	11.2
FC-NN from [HA21]	17,728	0.5
Proposed model	1,088	0.04

To conclude, we have proposed an ML-based mmWave beam prediction model that reduces the beam measurement overhead and predicts the transmit beam index with higher accuracy and lower computational complexity than the considered state-of-the-art approaches. The lower computational complexity of the proposed model results in reduced beam prediction time enabling faster prediction and faster retraining.

4.2 Evaluation of Full-duplex mmWave Massive MIMO Channel Estimation

In this section, we present our simulation results for SI and UE channel estimation. We compare channel estimators that we introduced in previous sections, i.e., LS, MMSE, and NN for different pilot dimensions. The normalized MSE (NMSE) is considered the performance metric to analyze the performance of the different channel estimators and it is defined as

$$\text{NMSE} = \mathbb{E}[\frac{||\mathbf{H_{true}}-\mathbf{H_{est}}||_F^2}{||\mathbf{H_{true}}||_F^2}] \tag{4.1}$$

where $\mathbf{H_{true}}$ and $\mathbf{H_{est}}$ are the true and estimated channel, respectively. We set the number of antenna elements of transmit and receive antenna arrays to 16, with a distance of 10λ between them, and antenna spacing in transmit and receive arrays is $d = \frac{\lambda}{2}$. The operating frequency is 28 GHz, corresponding to a wavelength of $\lambda = 10.71$ mm. The total number of downlink and uplink UEs is 8. The path loss parameters are based on experimental results from [S+16], where the path loss constant at the reference distance is $\Gamma = -72$ dB, the path loss exponent is $\eta = 2.92$, and the Shadow fading standard deviation is $\sigma_{sf} = 8.7$ dB. The number of multi-path components is $\mathrm{P} = 5$ and AS is $\theta_{AS} = 60°$. The SI Rician factor is $\mu = 40$ dB and we assume that the propagation SI cancellation is $\epsilon_{SI} = -40$ dB.

The NN-based channel estimators are trained on Python 3.9.13 and implemented using the Keras libraries with a TensorFlow backend in the Jupyter Notebook environment. We employ Adam optimizer with a batch size of 512 to update the network parameters. A dataset of 50000 samples is collected based on the channel model and it is split into 20,000 samples for training, 20,000 samples for validation, and 10,000 samples for testing. The validation dataset is used to ensure that the model does not simply memorize the training data but learns meaningful aspects of the data for effective prediction.

4.2.1 Analyzing NN-based Channel Estimator

Before examining the different channel estimators for various pilot dimensions. We conducted several experiments to understand the behavior of NN-based channel estimators under different channel conditions and NN architectures for training. The following results are specific to SI channel estimation with a pilot dimension of $\tau = N_t + K$. However, the same conclusions can be drawn for other pilot dimensions and UE channel estimations. For the sake of brevity, we have not included plots for other pilot dimensions and UE channel estimation. Throughout our simulation, we assume perfect knowledge of the channel covariance matrix for the MMSE channel estimator to compare the NN-based estimator with the best case of MMSE estimation.

Figure 13 illustrates the $\mathrm{NMSE}_{\mathrm{SI}}$ versus $\mathrm{SNR}_{\mathrm{SI}}$ with different numbers of hidden layers and $\mathrm{SNR}_{\mathrm{train}}$. Due to the discrepancy between SNR during the training and testing phases, the results slightly differ for different $\mathrm{SNR}_{\mathrm{train}}$. It is evident that training in a specific SNR regime yields slightly better performance in that regime. However, a significant gap can be observed with high $\mathrm{SNR}_{\mathrm{train}}$. Furthermore, we observe that the simplest CNN architecture, without any hidden layers and with just two convolutional kernels, outperforms CNNs with more hidden layers at high SNRs, while the NMSE is slightly worse at low SNRs. This observation suggests that incorporating more hidden layers in data-driven DNN-based channel estimation does not provide significant improvement. In fact, in high SNRs, it may lead to a deterioration in NMSE. It is important to note that we have explored other CNN architectures for this problem, such as CNN autoencoder, and observed the same behavior.

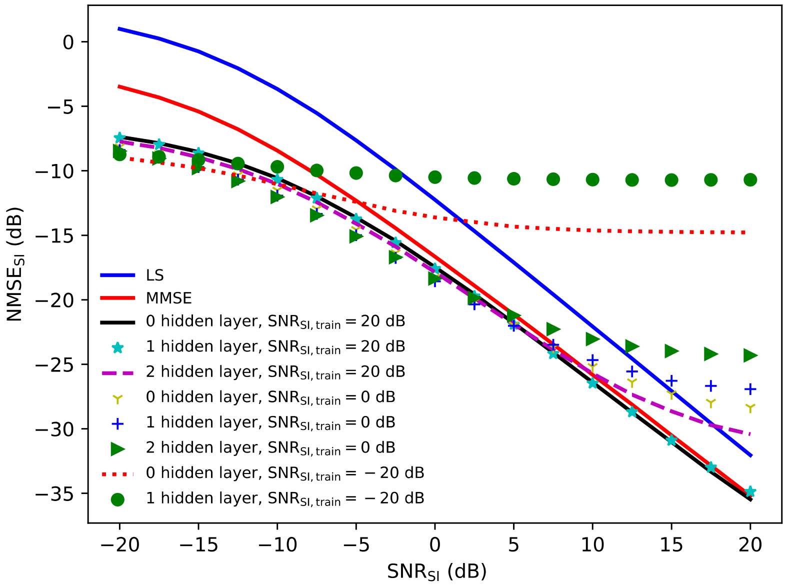

Figure 13: NMSE_{SI} versus SNR_{SI} for different SNR_{train} and hidden layers.

The results above represent the performance for fundamental channel estimation problem in multi-antenna systems, where the relationship between the received pilot signal and the channel is assumed to be linear. However, in practical scenarios, various non-linear distortions in hardware components exist, which adds complexity to this problem. This raises doubts about the applicability of the previous conclusion when the received pilot signal is affected by non-linear effects. To address this question, we consider the introduction of 1-bit ADCs at the BS to incorporate a non-linear distortion effect into the received pilot signal. When employing 1-bit ADCs, the received pilot signal will be

$$\mathbf{Y_{1-bit}} = \operatorname{sgn}(\mathbf{Y_{SI}}) \tag{4.2}$$

where $\operatorname{sgn}(.)$ is the element-wise signum function. Once again, we apply CNN with a varying number of hidden layers and SNR$_{\text{train}}$ to address the channel estimation problem with 1-bit ADCs. In this case, the input to the CNN is $\hat{\mathbf{Y}}_{\mathbf{1-bit}} = \mathbf{Y_{1-bit}} \mathbf{W}^{\mathbf{H}}_{\mathbf{N_t} \times \tau}$, and the output is the estimated channel. Figure 14 presents the NMSE of the LS, MMSE, and CNN-based channel estimators. As observed from this figure, the addition of hidden layers hardly improves the quality of channel estimation in this scenario. Therefore, even in the case of 1-bit ADCs, where the relation between the received pilot signal and the channel is non-linear, incorporating non-linear hidden layers does not significantly improve the prediction.

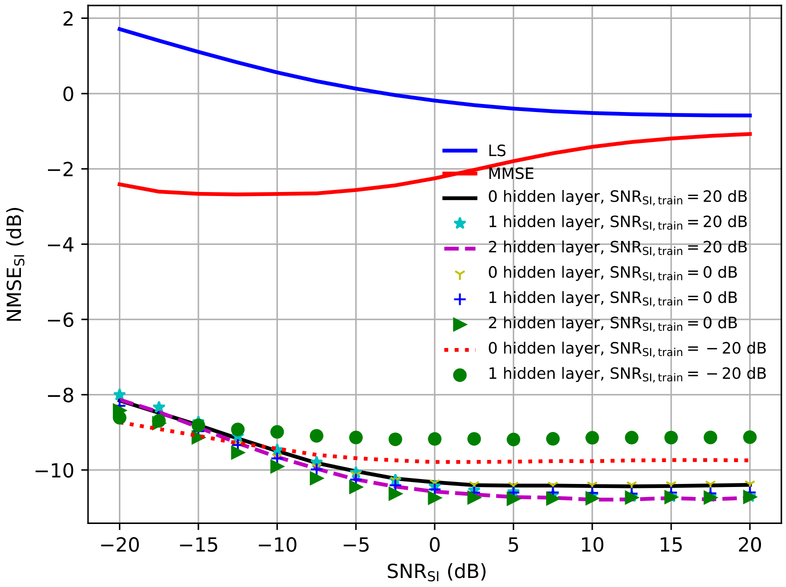

Figure 14: NMSE$_{SI}$ versus SNR$_{SI}$ for 1-bit ADC BS for different SNR$_{train}$ and hidden layers.

For the next experiment, we examine the behavior of the NN-based channel estimator under two different spatial channel correlation conditions: highly correlated channels and low correlated channels. The plots in Figure 15 illustrate how the LS, MMSE, and NN-based estimators perform under different spatial channel correlation strengths. In the highly correlated scenario, the MMSE estimator can leverage the perfect channel covariance matrix, resulting in a significant improvement in estimation quality. This leads to a substantial gap between the LS and MMSE estimations. However, in an uncorrelated channel, both the LS and MMSE estimations converge to the same NMSE at high SNRs. Comparing the NN-based estimation with the LS and MMSE estimations in both low correlated and highly correlated channel conditions provides interesting insights into the behavior of the NN-based estimator. In the uncorrelated scenario, the NN-based estimator outperforms both the MMSE and LS estimations. However, in highly correlated channel conditions, the MMSE estimator consistently outperforms the NN-based estimator. This observation suggests that the NN-based estimator, in a data-driven manner, is not capable of utilizing the second-order statistics of the channel for estimation, as the MMSE estimator does.

Furthermore, when comparing the NN-based estimator with the LS and MMSE estimators at low SNRs in highly correlated scenarios, it indicates that the NN performs well in handling noise.

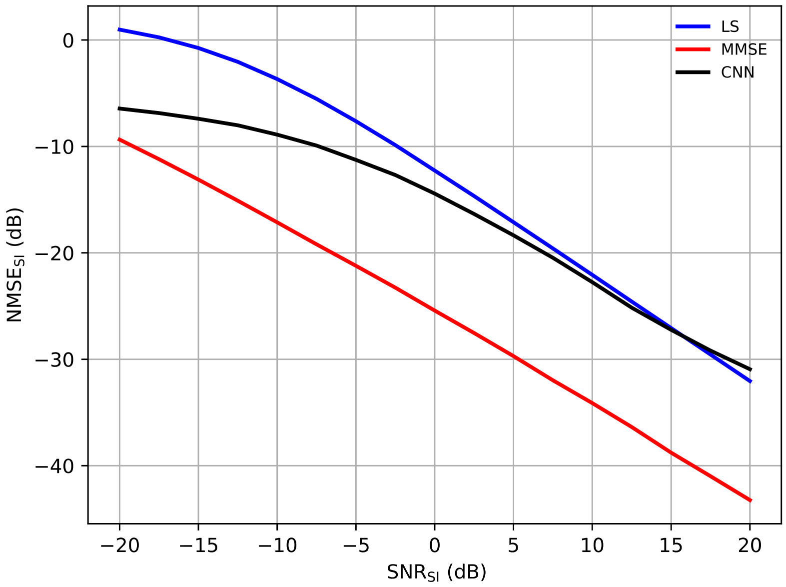

(a)

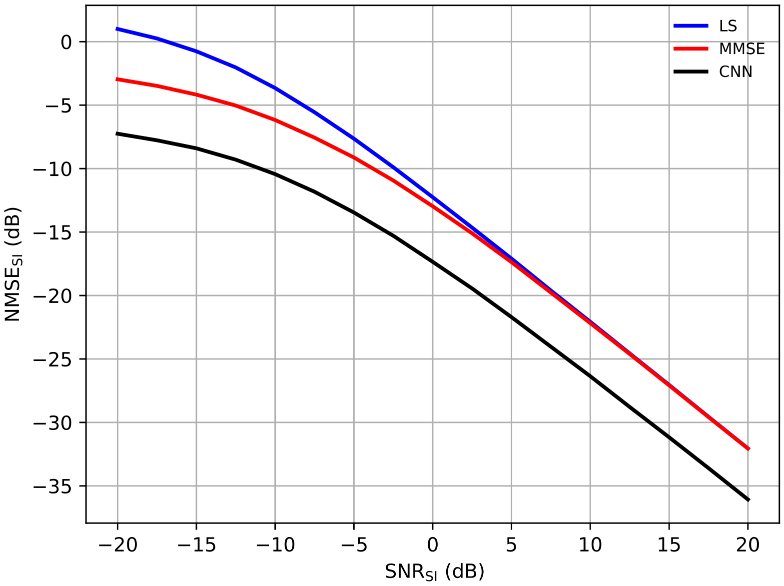

(b)

Figure 15: NMSE$_{SI}$ versus SNR$_{SI}$ for (a) uncorrelated channel and (b) highly correlated channel.

4.2.2 SI and UE Channel Estimation for Different Pilot Dimensions

In the figures presented below, we examine the performance of SI estimations for different pilot dimensions. For this simulation, we have set $\theta_{AS} = \frac{\pi}{3}$ and trained CNNs at an SNR of 20 dB. The NMSE of SI channel estimation vs SNR$_{SI}$ and SNR$_{UE}$ are provided in the following figures for different pilot dimensions, respectively. The results demonstrate that the CNN-based estimator outperforms the LS and MMSE estimators across all pilot dimensions. Moreover, from Figure 17, it is evident that the CNN-based approach is more resilient to interference from UEs when compared to the MMSE and LS estimation methods.

Using fewer pilot dimensions leads to a significant reduction in the quality of channel estimates for the CNN, MMSE, and LS-based approaches. However, this reduction in pilot dimensions results in saving more resources that can be allocated to transmitting payload data. The trade-off between the performance of channel estimates and the number of pilot dimensions used depends on the required accuracy threshold for channel estimates and the system data rate.

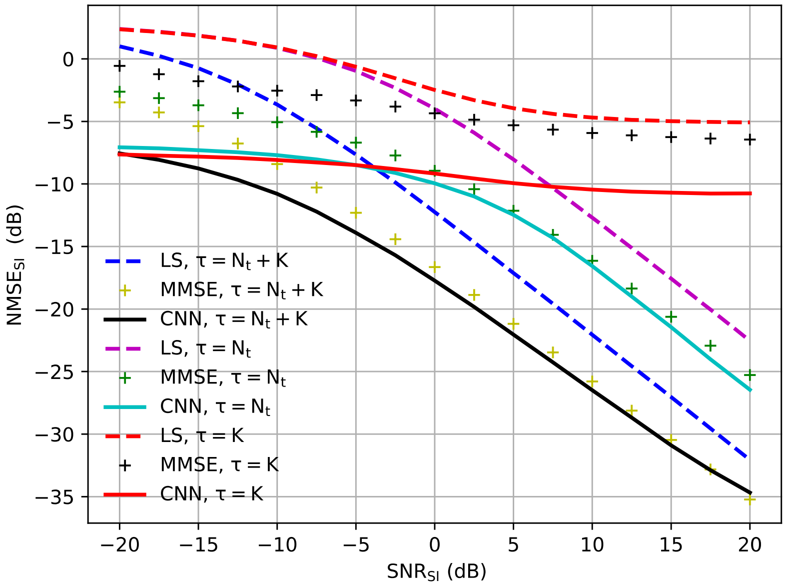

Figure 16: NMSE$_{SI}$ versus SNR$_{SI}$ for different pilot dimensions, SNR$_{UE}$ = 0 dB.

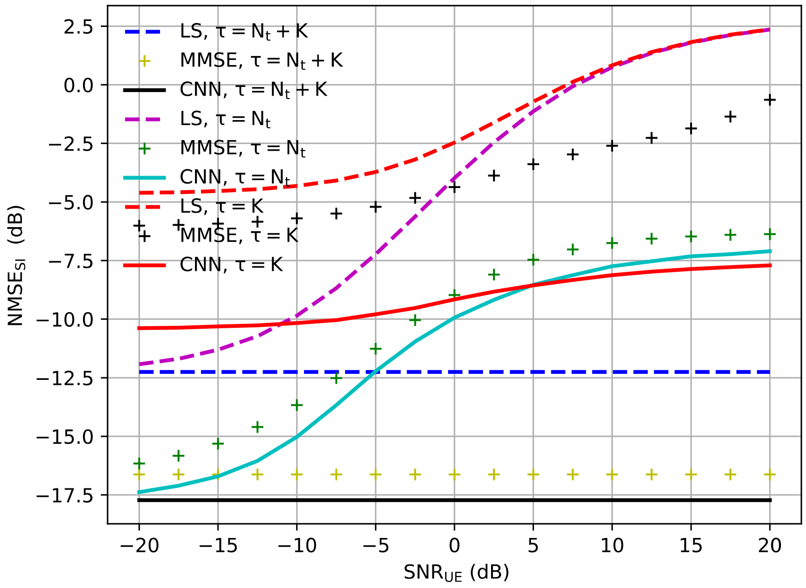

Figure 17: NMSE$_{SI}$ versus SNR$_{UE}$ for different pilot dimensions, SNR$_{SI}$ = 0 dB.

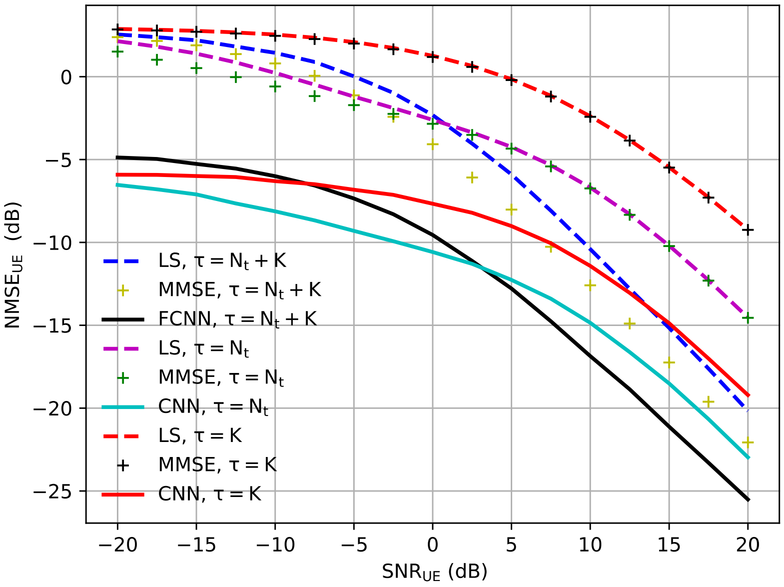

Figure 18: NMSE$_{SI}$ versus SNR$_{UE}$ for different pilot dimensions, SNR$_{SI}$ = 10 dB.

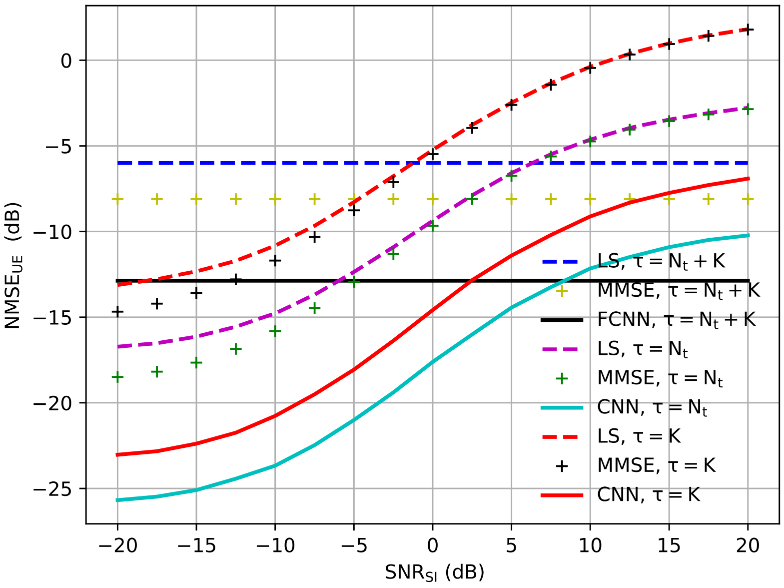

Figure 19: NMSE$_{SI}$ versus SNR$_{SI}$ for different pilot dimensions, SNR$_{UE}$ = 5 dB.

We have also generated similar plots for UE channel estimation, showing the NMSE with respect to SNR$_{UE}$ and SNR$_{SI}$. The plots are presented in Figure 18 and Figure 19 respectively, with varying pilot dimensions.

From the results, it is evident that the CNN-based approach using shorter pilot dimensions like $\tau = N_t$ or $\tau = K$ outperforms LS channel estimation with longer pilot dimensions $\tau = N_t + K$. Even MMSE channel estimator, when provided with perfect channel covariance matrix knowledge and longer pilot dimensions (e.g., $\tau = N_t + K$), is unable to outperform the CNN-based technique with shorter pilot dimensions (e.g., $\tau = N_t$). These findings clearly demonstrate the superiority of CNN in accurately estimating wireless channels, particularly in scenarios with lower SNRs and higher interference.

To further analyze the effect of SI cancelation on UE channel estimation, we conducted another experiment for the pilot dimension $\tau = K$. We considered two cases where for the first case, we cancel out the effect of the SI signal from the received pilot signal with the estimated SI channel while in the second scenario, we estimate UE channels in the presence of interference from the SI channel. The results are shown in Figure 20. Note that when calculating the MMSE estimation, in the case of SI cancelation, we incorporate the error covariance matrix of the estimated SI channel together with the covariance matrix of the UE channels while for the scenario without SI cancelation, we exploit the covariance matrix of both SI and UE channels. We can observe that MMSE estimations for these two scenarios result in the same NMSE of UE channel estimates. By comparing the results for LS, MMSE, and CNN channel estimators, we can realize that the SI cancelation during the pilot transmission phase does not provide significant improvement.

To examine the performance of NN-based channel mapping between receive and transmit antenna arrays at BS with a separate antenna configuration, we plotted the NMSE of this mapping with respect to varying angular spread and two different numbers of antennas in Figure 21. We trained an FCNN without hidden layers at $[10, 100, 190, 280]$ degrees of angular spread during the training. From this figure, it is evident that NN is able to predict the channel between transmit antenna arrays and UEs from the channel between receive antenna arrays and UEs. The prediction is more accurate in lower angular spread due to higher spatial correlation and vice versa. Furthermore, increasing the number of antennas improves the quality of prediction as angular regulation increases when employing a larger number of antenna arrays.

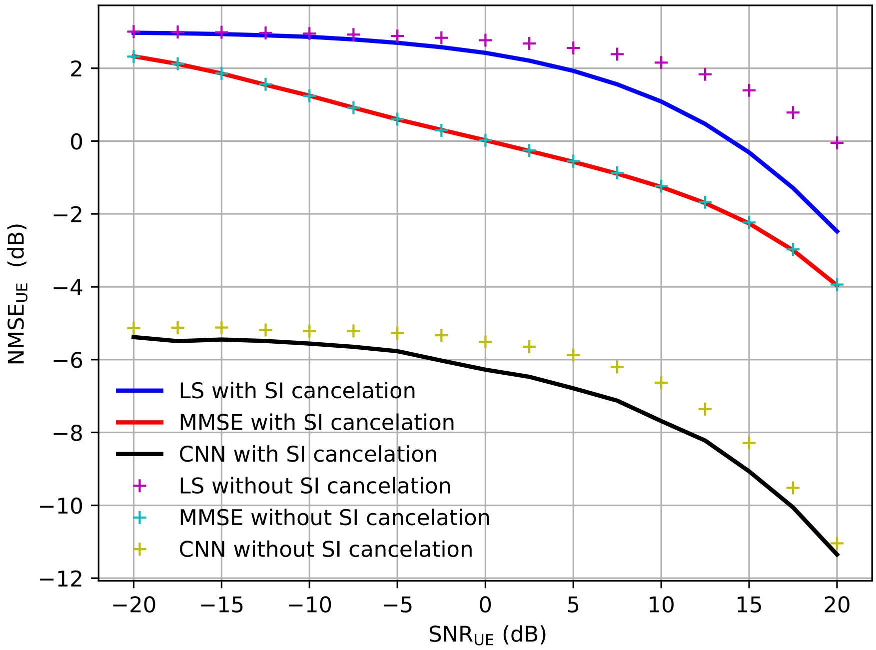

Figure 20: UE channel estimation with/without SI cancelation τ = K, SNR_{SI} = 20 dB.

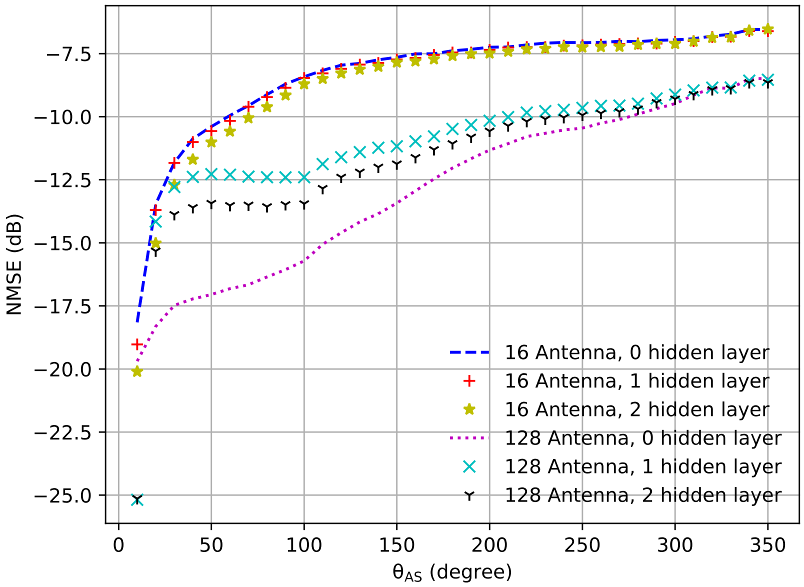

Figure 21: NMSE of channel mapping between receive and transmit antenna arrays vs angular spread.

Finally, we compare the computational complexity of LS, MMSE, and NN channel estimators in terms of complex multiplications. The results are summarized in Table 4 and a bar plot is given in Figure 22 for SI channel estimation and pilot dimension $\tau = N_t$. Note that we have ignored the computational complexity of the covariance matrix calculation for MMSE estimation, as the channel statistics do not typically change during several coherence blocks. For the same reasons, we also ignored the computational complexity of the matrices in the MMSE formula that depend on spatial correlation matrices, assuming they can be pre-computed and used until the channel statistics change substantially. For NN, we reported the computational complexity of a CNN network without hidden layers.

According to Table 4, the number of complex multiplications exhibits quadratic growth with the number of received antennas in MMSE estimation, while for LS and NN-based estimation, it is linear. Furthermore, due to employing a basic NN architecture, the added computational complexity for the NN estimator is only slightly higher than LS estimation.

Table 4: Number of complex multiplications for LS, MMSE and NN estimators.

	LS	**MMSE**	**NN**
SI	$N_r N_t \tau$	$N_r^2 N_t \tau$	$N_r N_t \tau$+36$N_r N_t$
UE	$N_r \mathrm{K} \tau$	$N_r^2 \mathrm{K} \tau$	$N_r \mathrm{K} \tau$+36$N_r \mathrm{K}$

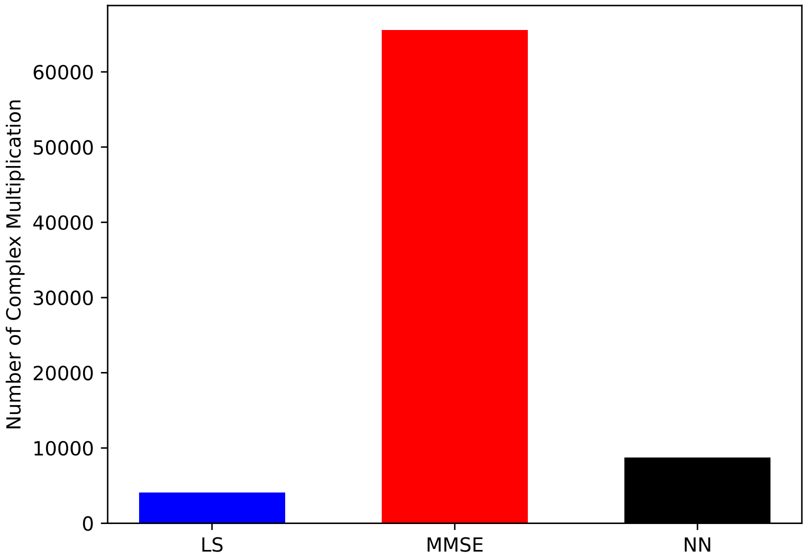

Figure 22: Number of complex multiplications for SI channel estimation of different estimators.

4.3 Evaluation of Non-orthogonal Multiple Access

In this section, we study the relative performance of the considered system with an A-RIS, with a conventional phase-only RIS, and without any kind of RIS.

We assume that all channels in our system model illustrated in Figure 3 are Rayleigh fading, but with different channel gains, and we solve the optimization problem (3.40) using the parameters in Table 5. In the results, we present the required total power for the two UEs to meet the target SINRs T_1 and T_2 normalized with the BS noise, i.e. $(p_1 + p_2)/\sigma^2$. In all the presented results, the resulting SINRs γ_1 and γ_2 for UE_1 and UE_2, respectively, are verified to satisfy the targets T_1 and T_2, respectively. In fact, T_1 and T_2 are met with equality, which indicates the optimality of the numerical optimization results.

Table 5: Summary of key parameters for non-orthogonal multiple access evaluation.

Variable	**Description**	**Value**
σ^2	AWGN power at BS receiver	1
P_{j}/σ^2	Normalized jammer antenna power	40
$\mathbb{E}\{h_1\}$	Gain between UE_1 & BS	5
$\mathbb{E}\{h_2\}$	Gain between UE_2 & BS	2
$\mathbb{E}\{\mathbf{h}_{\mathrm{j}}(:)\}$	Gain between jammer & RIS	1
$\mathbb{E}\{\mathbf{g_1}(:)\}$	Gain between UE_1 & RIS	1
$\mathbb{E}\{\mathbf{g_2}(:)\}$	Gain between UE_2 & RIS	0.2
$\mathbb{E}\{\mathbf{G}_{\mathrm{j}}(:,:)\}$	Gain between jammer & RIS	0.2
$\mathbb{E}\{\mathbf{f}(:)\}$	Gain between RIS & BS	1
T_1	Targeted SINR threshold for UE_1	5
T_2	Targeted SINR threshold for UE_2	5

In Figure 23, we show the resulting required total transmit power as a function of the number of RIS elements in the presence of a jammer with $M = 4$ antennas. As it can be seen, a regular non-absorbing RIS is beneficial compared with no RIS provided the RIS is equipped with more than $N = 2$ elements, whereas the A-RIS has a performance gain for all considered $N = 2$.

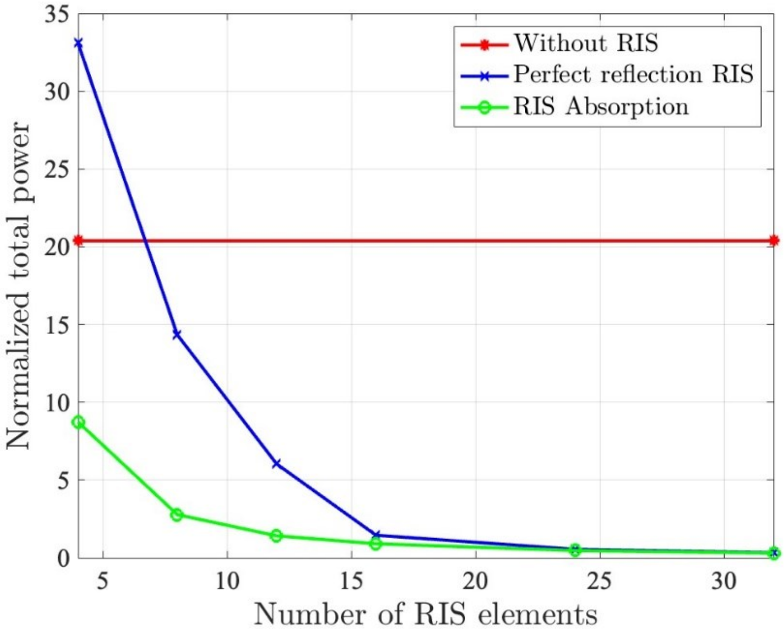

Figure 23: Required total transmit power to meet the user quality of service requirements in the presence of a jammer with M = 4 antennas, as a function of the number of RIS elements.

In Figure 24 and Figure 25, we show the corresponding results for a jammer with $M = 8$ and $M = 16$ elements, respectively. The relative performance for the no RIS, regular RIS, and A-RIS is the same, but due to the stronger jammer, the crossing point for the regular RIS increases with the number of jammer antennas M. It is also interesting to note that, compared to the no RIS case, the required total transmit power more than doubles when the number of jammer antennas is increased from $M = 4$ to $M = 8$ although the total jammer power is only doubled. That can likely be explained by the additional beamforming gain for the jammer. Increasing the number of jammer antennas from $M = 8$ to $M = 16$ results in just slightly more than doubled the required total transmit power, which can most likely be explained by saturation in the beamforming gain. Another interesting observation is that when the RIS is very small, e.g., with only 4 or 8 elements, the performance with a conventional phase-only RIS is actually worse than if no RIS were present at all. This is because the conventional RIS does not have a sufficient number of degrees of freedom to eliminate the interference, and its presence as a reflector only serves to actually increase the interference seen by the BS. The A-RIS is able to control the amount of reflected energy in addition to the phase shifts and thus does not suffer from this drawback.

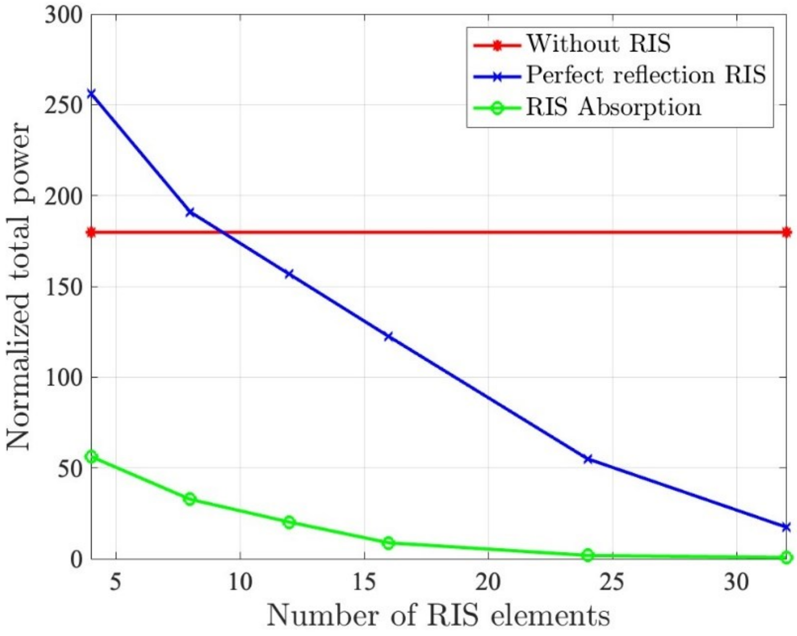

Figure 24: Required total transmit power to meet the user quality of service requirements in the presence of a jammer with M = 8 antennas, as a function of the number of RIS elements.

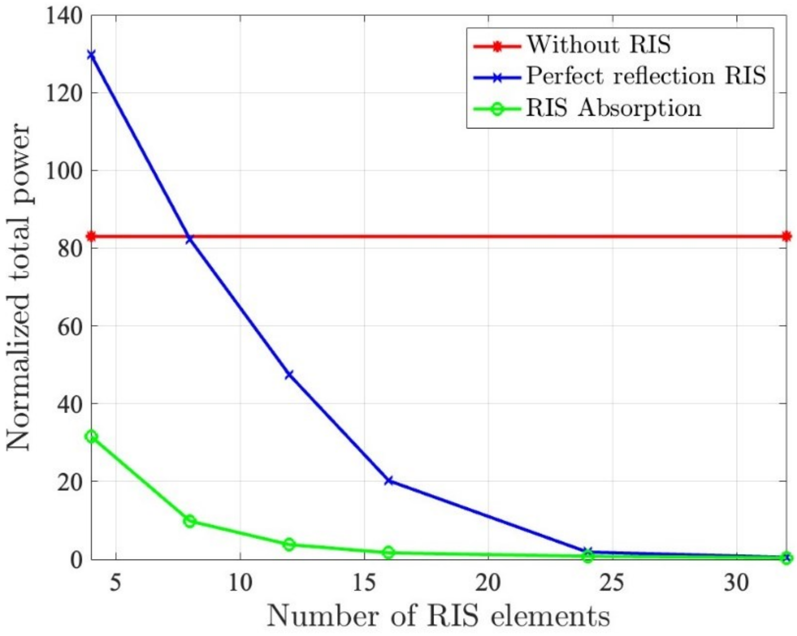

Figure 25: Required total transmit power to meet the user quality of service requirements in the presence of a jammer with M = 16 antennas, as a function of the number of RIS elements.

In Figure 26, we show the resulting average absorption level of the A-RIS as a function of the number of A-RIS elements in the presence of a jammer with $M = 4, 8, 16$ antennas. As it can be seen, the absorption capability of the A-RIS is very useful when the degrees of freedom required for the A-RIS to mitigate the jammer is low, i.e., when the number of A-RIS elements N is small compared to the number of jammer antennas M. With increasing N, the average absorption level of the A-RIS elements is monotonically decreasing, and thus the operation of the A-RIS approaches that of the regular non-absorbing RIS, which is in line with the results in Figure 23 to Figure 25 showing that the performance of a conventional RIS is approaching the performance of the A-RIS as the number of elements increases.

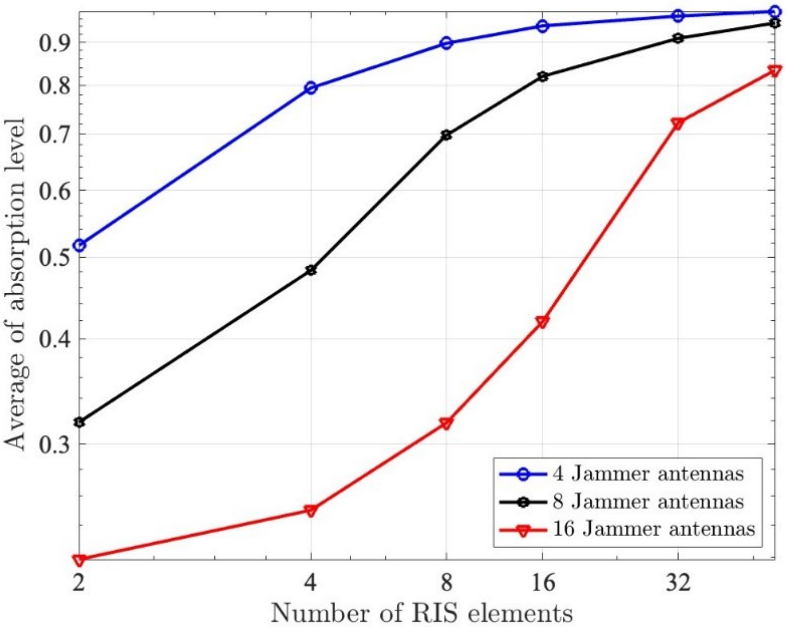

Figure 26: Resulting average absorption level of the A-RIS as a function of the number of A-RIS elements in the presence of a jammer with M = 4, 6, 16 antennas.

Finally, in Figure 27, we show the total transmit power required to meet the user quality of service requirements as a function of the number of jammer antennas for the cases of no RIS, a conventional RIS, and an A-RIS, both with $N = 16$ elements. It can be observed that the greater the number of jammer antennas, the more beneficial is the use of RIS technology, and the additional benefits of RIS absorption rapidly increases when the number of jammer antennas is more than $M = 4$.

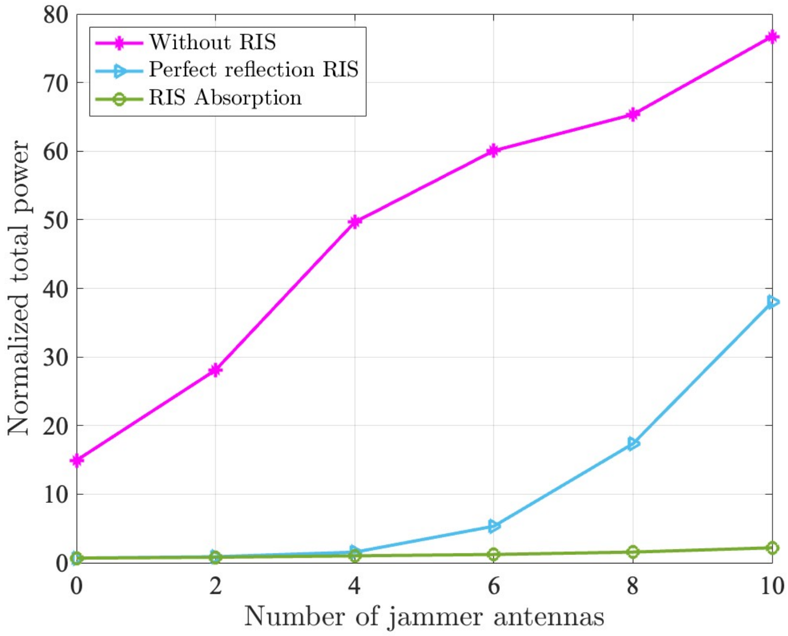

Figure 27: Required total transmit power to meet the user quality of service requirements, as a function of the number of jammer antennas, for the cases of no RIS, a regular RIS, and an A-RIS, both with N = 16 elements.

4.4 Evaluation of Integrated Backhaul and Access

In this section, we evaluate the performance of our proposed algorithm for distributed resource allocation in IAB networks. A simulation setup is created to emulate an IAB HetNet topology consisting of multiple macro and small base stations.

4.4.1 Simulation and Primary Results

The primary goal is to satisfy the SBS load as much as possible while considering achieving load balance for the MBS donor nodes. Figure 28 shows the load on the donor nodes. In the proposed method, the figure shows that the load is balanced as the percentage usage is similar and there is no significant discrepancy in the distribution of the load. However, in the random resources allocation method, some donor nodes are fully occupied while others are not, leading to an unbalanced load distribution.

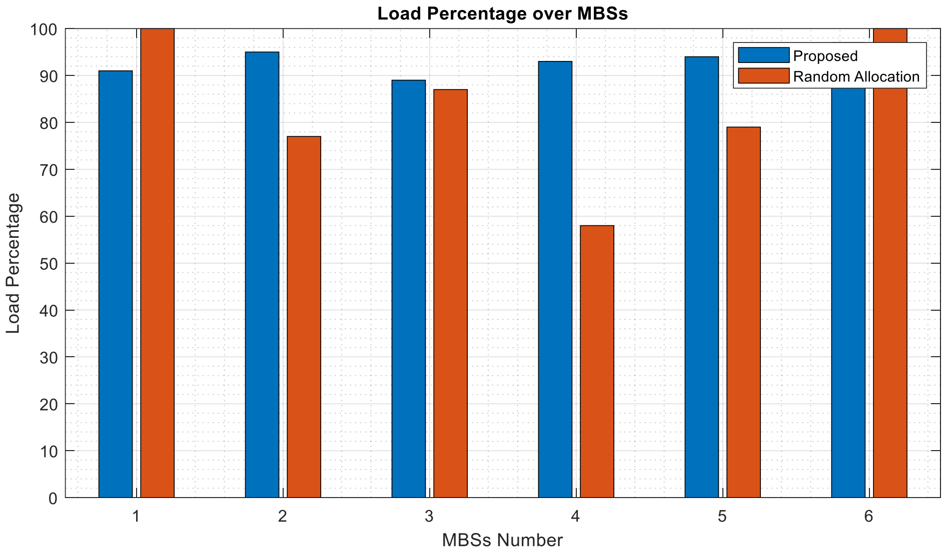

Figure 28: Load percentage over the donor nodes.

Figure 29 shows that the load of each SBS is served in the proposed method by ensuring complete offloading for all nodes, while in random allocation, many SBSs nodes are not perfectly served as a result of the misdistribution of the connection between the SBSs nodes and the MBSs.

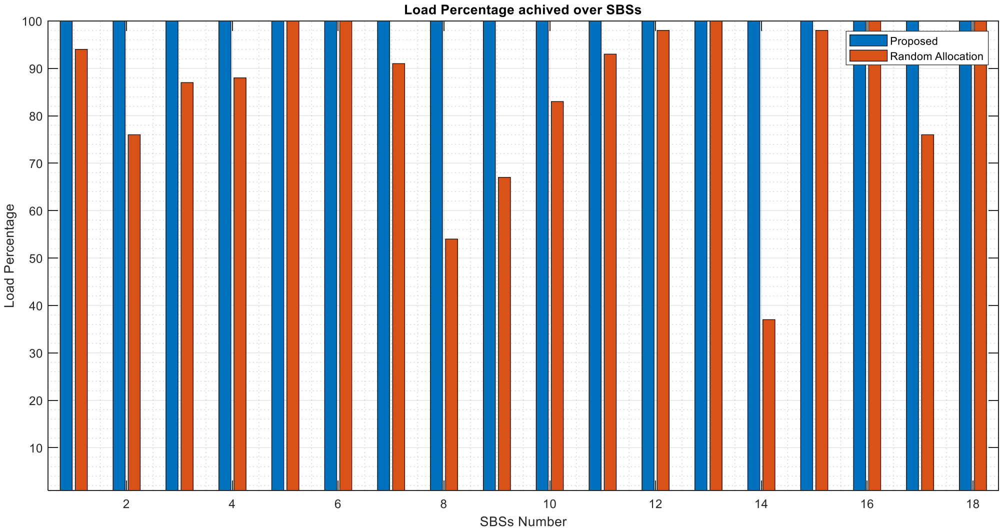

Figure 29: Load percentage over the IAB nodes.

From the previous two figures, we conclude that the SBS nodes are connected almost ideally with the donor nodes using the proposed method; the load of the SBS is served without reaching a bottleneck state for the donor nodes.

5 Research Progress and Next Steps

5.1 Machine Learning based mmWave Beam Management

Due to the late start of ESR, we started our investigations of ML based BM at the beginning of 2022. We started our study with the detailed literature survey, the outcome of this phase was delivered in D1.2 and has been published in IEEE open access journal [KGP+23]. After completing the detailed literature survey, we started developing our simulation setup. The simulation setup is developed in MATLAB in combination with Pytorch for ML models. We simulated two traditional BM approaches namely EBS and HBS, which serve as a baseline for comparison with ML based BM approaches. Additionally, we also simulated two selected state-of-the-art ML based BM approaches from [ECB+21], and [HA21]. After having necessary simulation capabilities, we started working on spatial domain mmWave beam prediction and proposed a low-complexity beam prediction model, whose details are provided above. The proposed low-complexity ML model for mmWave beam prediction has been submitted to IEEE journal for publication.

In summary, we have investigated the spatial domain beam prediction, which focuses on indoor environments and lower mobility scenarios. Higher mobility in outdoor environments requires beam prediction in temporal domain. Thus, the next step in our study is to evaluate the temporal domain beam prediction for ML based mmWave beam prediction. Some of the most common ML models that can be used for temporal domain beam prediction include RNN, LSTM networks and artificial intelligence transformers. We plan to study these models in our next steps. Finally, to cope up with everchanging wireless environments, we plan to study reinforcements learning based ML model for mmWave beam management.

5.2 Full-duplex mmWave Massive MIMO Channel Estimation

We have studied the channel estimation problem for full-duplex mmWave massive MIMO systems using NNs. The interference caused by simultaneous transmissions and receptions in full-duplex systems poses a significant challenge which makes SI channel estimation a critical problem for enabling full-duplex systems. Due to the large antenna arrays, SI is a large MIMO channel, making its resource estimation intensive in terms of time and frequency.

To address the pilot overhead associated with SI channel estimation, we shared pilot resources between the transmit antenna arrays at the full-duplex BS and UEs. We explored different pilot dimensions and compared the performance of LS, MMSE, and NN-based channel estimation techniques in terms of NMSE.

Furthermore, we conducted different experiments, such as varying the number of hidden layers, training SNR, introducing non-linear distortion in the received pilot signal, and examining channel spatial correlation strength, to understand how NNs perform channel estimation in various scenarios. Based on our experiments, we observed that using deep NNs with non-linear hidden layers is not beneficial for channel estimation problems. Moreover, we found that NNs employing a data-driven approach do not fully leverage spatial correlation compared to the MMSE estimator in highly correlated wireless channels. However, in scenarios where spatial correlation is not extremely high, our results demonstrated that NNs can outperform MMSE estimation, especially when using very low pilot dimensions. This performance allows for a reduction in pilot overhead in full-duplex systems and enables approaching the same pilot overhead levels required in half-duplex systems. Moreover, we introduced RX-TX channel mapping for separate antenna configurations in full-duplex systems. To approximate this mapping, we used NNs, and the simulation results demonstrated that NNs can effectively map channels from receive antenna arrays to transmit antenna arrays, particularly in scenarios with high correlation and large antenna arrays.

Lastly, our calculations of the computational complexity for LS, MMSE, and NN channel estimators revealed that NN-based estimation requires fewer complex multiplications compared to MMSE estimation with perfect knowledge of the channel covariance matrix.

For the future works, we aim to focus CSI feedback in massive MIMO systems. To combat the problem of retraining a deep learning model when channel statistics changes noticeably, we propose to study an instance adaptive deep learning-based CSI compression technique.

5.3 Non-orthogonal Multiple Access

We started our research on NOMA in late 2020. We started our study with a detailed literature review of NOMA and RIS. In the second year, we minimized the total power transmitted by the user terminals under quality-of-service constraints by controlling the propagation from the users to the base station with the help of the RIS. Also, we published a conference paper in WCNC. Our next aim is to extend our system model and use different toolboxes for solving our problem formulation. In particular, we are working on more advanced optimization techniques in order to address more complex scenarios, such as RIS with hundreds of elements, multi-antenna base station and more users. A journal paper is under submission.

5.4 Resources allocation in IAB networks

Due to the late start of ESR, we started our investigations of IAB in mobile networks in May 2022. We started our study with the detailed literature survey, the outcome of this phase was delivered in D1.2.

After completing the detailed literature survey, we started developing our simulation setup. The simulation setup is developed in MATLAB, the setup has been created to emulate an IAB HetNet topology consisting of multiple macro and small base stations, and compare the new resource allocation algorithm with the random resource allocation. We plan to study the evaluation metrics in our next steps and the proposed Stackelberg game-based approach for distributed resource allocation in IAB networks. The key performance metrics like throughput, load balancing, latency etc. will be used to analyze the equilibrium and compare it with other benchmark approaches. Specifically, the following metrics will be considered for performance analysis:

- Throughput cumulative distribution function (CDF): Analyze the CDF of throughput achieved at different nodes to evaluate fairness.
- Load balancing: The load distribution across macro base stations will be studied to demonstrate the ability of the proposed approach to balance load in the network.
- Network throughput vs number of nodes: This metric captures how total network throughput will be scaled with increasing node density.
- Average node throughput vs network load: This analyzes the impact of varying total network traffic load on per-node performance.
- Latency vs number of hops: End-to-end latency for flows traversing with different hop counts will be evaluated to study the effect of multi-hop routing.
- Outage probability vs node density: These metric measures redundancy and reliability under different deployment densities.
- Utility vs iterations: Convergence behavior of the iterative algorithm will be demonstrated by plotting change in total network utility over iterations.

The above performance metrics will be presented, compared against baseline schemes, and analyzed to validate the effectiveness of the proposed approach. Results will then be submitted to a proper journal.

6 Conclusions

In this deliverable, we have reported on the progress of the SEMANTIC ESRs contributions towards the objectives of WP1 (Spectrum and Forward-Compatibility Aspects for multi-GHz NR operation).

Key findings and intermediate performance evaluation results were reported. This includes results on beam-based transmissions in multi-GHz bands; low-complexity techniques for channel estimation in massive MIMO in the mmWave band; distributed MIMO with focus on IAB; and NOMA for enhancing user experience in beyond 5G systems.

Bibliography

[3GP+20] 3GPP TS 38.801 V16.2.0 (2020-12) Study on new radio (NR) access technology.

[3GP+22] 3GPP, “Study on channel model for frequencies from 0.5 to 100 GHz,” TR 38.901 V17.0, 2022.

[AA19] M. Alrabeiah and A. Alkhateeb, "Deep Learning for TDD and FDD Massive MIMO: Mapping Channels in Space and Frequency," 2019 53rd Asilomar Conference on Signals, Systems, and Computers, Pacific Grove, CA, USA, 2019, pp. 1465-1470, doi: 10.1109/IEEECONF44664.2019.9048929.

[ADS+22] A. Albanese, F. Devoti, V. Sciancalepore, M. Di Renzo, and X. Costa-Perez, “MARISA: A self-configuring metasurfaces absorption and reflection solution towards 6G,” in IEEE International Conference on Computer Communications (INFOCOM), 2022, pp. 250–259.

[AH22] Alghafari, H. and Haghighi, M.S., 2022. Decentralized joint resource allocation and path selection in multi-hop integrated access backhaul 5G networks. Computer Networks, 207, p.108837.

[AHS+22] D. Adesina, C.-C. Hsieh, Y. E. Sagduyu and L. Qian, “Adversarial Machine Learning in Wireless Communications using RF Data: A Review,” *IEEE Communications Surveys & Tutorials*, no. 1-1, 2022.

[BH+14] F. Boccardi, R. W. Heath, A. Lozano, T. L. Marzetta and P. Popovski, "Five disruptive technology directions for 5G," in IEEE Communications Magazine, vol. 52, no. 2, pp. 74-80, February 2014, doi: 10.1109/MCOM.2014.6736746.

[CRJ19] S. -E. Chiu, N. Ronquillo and T. Javidi, "Active Learning and CSI Acquisition for mmWave Initial Alignment," in IEEE Journal on Selected Areas in Communications, vol. 37, no. 11, pp. 2474-2489, Nov. 2019, doi: 10.1109/JSAC.2019.2933967.

[DA22] U. Demirhan and A. Alkhateeb, Integrated sensing and communication for 6G: Ten key machine learning roles, *arXiv preprint* arXiv:2208.02157, 2022.

[ECB+21] H. Echigo, Y. Cao, M. Bouazizi and T. Ohtsuki, "A Deep Learning-Based Low Overhead Beam Selection in mmWave Communications," in IEEE Transactions on Vehicular Technology, vol. 70, no. 1, pp. 682-691, Jan. 2021, doi: 10.1109/TVT.2021.3049380.

[ES+14] E. Everett, A. Sahai and A. Sabharwal, "Passive Self-Interference Suppression for Full-Duplex Infrastructure Nodes," in IEEE Transactions on Wireless Communications, vol. 13, no. 2, pp. 680-694, February 2014, doi: 10.1109/TWC.2013.010214.130226.

GPR+19 M. Giordani, M. Polese, A. Roy, D. Castor and M. Zorzi, "A Tutorial on Beam Management for 3GPP NR at mmWave Frequencies," in IEEE Communications Surveys & Tutorials, vol. 21, no. 1, pp. 173-196, Firstquarter 2019, doi: 10.1109/COMST.2018.2869411.

[HA21] Y. Heng and J. G. Andrews, "Machine Learning-Assisted Beam Alignment for mmWave Systems," in IEEE Transactions on Cognitive Communications and Networking, vol. 7, no. 4, pp. 1142-1155, Dec. 2021, doi: 10.1109/TCCN.2021.3078147.

[HCN+21] S. Hu, X. Chen, W. Ni, E. Hossain and X. Wang, “Distributed Machine Learning for Wireless Communication Networks: Techniques, Architectures, and Applications,” *IEEE Communications Surveys & Tutorials*, vol. 23, no. 3, pp. 1458-1493, 2021.

[HM19] M. Hussain and N. Michelusi, "Energy-Efficient Interactive Beam Alignment for Millimeter-Wave Networks," in IEEE Transactions on Wireless Communications, vol. 18, no. 2, pp. 838-851, Feb. 2019, doi: 10.1109/TWC.2018.2885041.

[IZD17] Islam, S. M., Zeng, M., & Dobre, O. A., “NOMA in 5G systems: Exciting possibilities for enhancing spectral efficiency,” IEEE 5G Tech Focus, vol. 1, p. 2, 2017.

KGP+23 M. Qurratulain Khan, A. Gaber, P. Schulz and G. Fettweis, "Machine Learning for Millimeter Wave and Terahertz Beam Management: A Survey and Open Challenges," in IEEE Access, vol. 11, pp. 11880-11902, 2023, doi: 10.1109/ACCESS.2023.3242582.

[KKI+21] J. Kaur, M. A. Khan, M. Iftikhar, M. Imran and Q. Emad Ul Haq, “Machine Learning Techniques for 5G and Beyond,” *IEEE Access*, vol. 9, pp. 23472-23488, 2021.

[IM22] I. Alamzadeh and M. F. Imani, “Sensing and reconfigurable reflection of electromagnetic waves from a metasurface with sparse sensing elements,” IEEE Access, vol. 10, pp. 105 954–105 965, 2022.

[KM+89] Hornik, Kurt, Maxwell Stinchcombe, and Halbert White. "Multilayer feedforward networks are universal approximators." *Neural networks* 2, no. 5 (1989): 359-366.

[LDT+21] Le, C. B., Do, D. T., Li, X., Huang, Y. F., Chen, H. C., & Voznak,
M. (2021). Enabling NOMA in backscatter reconfigurable intelligent surfaces-aided systems. IEEE Access, 9, 33782-33795

[LLM+21] Liu, Y., Liu, X., Mu, X., Hou, T., Xu, J., Di Renzo, M., & Al-Dhahir, N.(2021). Reconfigurable intelligent surfaces: Principles and opportunities. IEEE communications surveys & tutorials, 23(3), 1546-1577.

[LWS20] J. Y. Lai, W. -H. Wu and Y. T. Su, "Resource Allocation and Node Placement in Multi-Hop Heterogeneous Integrated-Access-and-Backhaul Networks," in IEEE Access, vol. 8, pp. 122937-122958, 2020

[MMF+20] C. Madapatha, B. Makki, C. Fang, O. Teyeb, E. Dahlman, M.-S. Alouini, and T. Svensson, “Integrated access and backhaul networks: Current status and potentials,” IEEE Open Journal of the Communications Society, 2020.

[MP05] M. Marcus and B. Pattan, "Millimeter wave propagation: spectrum management implications," in *IEEE Microwave*

Magazine, vol. 6, no. 2, pp. 54-62, June 2005, doi: 10.1109/MMW.2005.1491267.

[NKD15] Q. -U. -A. Nadeem, A. Kammoun, M. Debbah and M. -S. Alouini, "A Generalized Spatial Correlation Model for 3D MIMO Channels Based on the Fourier Coefficients of Power Spectrums," in IEEE Transactions on Signal Processing, vol. 63, no. 14, pp. 3671-3686, July15, 2015, doi: 10.1109/TSP.2015.2430841.

[PZP+22] M. Pagin, T. Zugno, M. Polese and M. Zorzi, "Resource Management for 5G NR Integrated Access and Backhaul: A Semi-Centralized Approach," in IEEE Transactions on Wireless Communications, vol. 21, no. 2, pp. 753-767, Feb. 2022.

[RA+21] I. P. Roberts, J. G. Andrews, H. B. Jain and S. Vishwanath, "Millimeter-Wave Full Duplex Radios: New Challenges and Techniques," in IEEE Wireless Communications, vol. 28, no. 1, pp. 36-43, February 2021, doi: 10.1109/MWC.001.2000221.

[RAP+13] T. S. Rappaport *et al*., "Millimeter Wave Mobile Communications for 5G Cellular: It Will Work!," in *IEEE Access*, vol. 1, pp. 335-349, 2013, doi: 10.1109/ACCESS.2013.2260813.

[ROH14] W. Roh et al., "Millimeter-wave beamforming as an enabling technology for 5G cellular communications: theoretical feasibility and prototype results," in IEEE Communications Magazine, vol. 52, no. 2, pp. 106-113, February 2014, doi: 10.1109/MCOM.2014.6736750.

[RPM+21] L. Rao, M. Pant, L. Malviya, A. Parmar and S. V. Charhate, “5G beamforming techniques for the coverage of intended directions in modern wireless communication: in-depth review,” *International Journal of Microwave and Wireless Technologies*, vol. 13, no. 10, pp. 1039-1062, 2021.

[RRE14] S. Rangan, T. S. Rappaport and E. Erkip, "Millimeter-Wave Cellular Wireless Networks: Potentials and Challenges," in *Proceedings of the IEEE*, vol. 102, no. 3, pp. 366-385, March 2014, doi: 10.1109/JPROC.2014.2299397.

[S+16] S. Sun et al., "Propagation Path Loss Models for 5G Urban Micro- and Macro-Cellular Scenarios," 2016 IEEE 83rd Vehicular Technology Conference (VTC Spring), Nanjing, China, 2016, pp. 1-6, doi: 10.1109/VTCSpring.2016.7504435.

[SAD18] C. Saha, M. Afshang, and Harpreet S. Dhillon “Bandwidth Partitioning and Downlink Analysis in mmWave Integrated Access and Backhaul for 5G,” IEEE Transactions on Wireless Communications, 2018.

[SD19] C. Saha and H. Dhillon, "Millimeter wave integrated access and backhaul in 5G: Performance analysis and design insights", IEEE J. Sel. Areas Commun., vol. 37, no. 12, pp. 2669-2684, Dec. 2019.

[SE+20] L. Sanguinetti, E. Björnson and J. Hoydis, "Toward Massive MIMO 2.0: Understanding Spatial Correlation, Interference Suppression, and Pilot Contamination," in IEEE Transactions on Communications, vol. 68, no. 1, pp. 232-257, Jan. 2020, doi: 10.1109/TCOMM.2019.2945792.

[SS+14] A. Sabharwal, P. Schniter, D. Guo, D. W. Bliss, S. Rangarajan and R. Wichman, "In-Band Full-Duplex Wireless: Challenges and Opportunities," in IEEE Journal on Selected Areas in Communications, vol. 32, no. 9, pp. 1637-1652, Sept. 2014, doi: 10.1109/JSAC.2014.2330193.

[SZS+18] Sadia, H., M. Zeeshan, and S.A. Sheikh, “Performance analysis of downlink power domain NOMA under fading channels,” in *2018 ELEKTRO*, 2018.

[TJ91] Thomas M. Cover, Joy A, Elements of information theory, *College of New York*, 1991.

[XRC+22] X. Hu, R. Zhang, and C. Zhong, “Semi-passive elements assisted channel estimation for intelligent reflecting surface-aided communications,”IEEE Trans. Wireless Commun., vol. 21, no. 2, pp. 1132–1142, Feb. 2022.

[XYS+21] Yuan, X., Zhang, Y. J. A., Shi, Y., Yan, W., & Liu, H. (2021).

Reconfigurable-intelligent-surface empowered wireless communications: Challenges and opportunities. IEEE wireless communications, 28(2),136-143.

[YRC22] Yin, H., Roy, S. and Cao, L., 2022. Routing and Resource Allocation for IAB Multi-Hop Network in 5G Advanced. IEEE Transactions on Communications, 70(10), pp.6704-6717.

[YXJ+21] Y. Liu, X. Mu, J. Xu, R. Schober, Y. Hao, H. V. Poor, and L. Hanzo,
”STAR: Simultaneous Transmission and Reflection for 360◦ coverage by intelligent surfaces,” IEEE Wireless Communications, vol. 28, no. 6, pp. 102–109, 2021

[YXY+21] Yang, G., Xu, X., Liang, Y. C., & Di Renzo, M. (2021). Reconfigurable intelligent surface-assisted non-orthogonal multiple access. IEEE Transactions on Wireless Communications, 20(5), 3137-3151.

[YYA+13] Y. Saito, Y. Kishiyama, A. Benjebbour, T. Nakamura, A. Li and K. Higuchi, "Non-Orthogonal Multiple Access (NOMA) for Cellular Future Radio Access," *2013 IEEE 77th Vehicular Technology Conference (VTC Spring)*, 2013, pp. 1-5, doi: 10.1109/VTCSpring.2013.6692652.

ZDF+21 Zhang, B., Devoti, F., Filippini, I. and De Donno, D., 2021. Resource allocation in mmWave 5G IAB networks: A reinforcement learning approach based on column generation. Computer Networks, 196, p.108248.